Advanced Drug Delivery Reviews 89 (2015) 71–90

Contents lists available at ScienceDirect

Advanced Drug Delivery Reviews

journal homepage: www.elsevier.com/locate/addr

Raman microscopy for cellular investigations — From single cell imaging to drug carrier uptake visualization☆

Birthe Kann[a,b], Herman L. Offerhaus[b], Maike Windbergs[a,c,*], Cees Otto[d,**]

[a] Saarland University, Department of Biopharmaceutics and Pharmaceutical Technology, Campus A4.1, 66123 Saarbruecken, Germany
[b] University of Twente, Optical Sciences Group, MESA + Institute for Nanotechnology, P.O. Box 217, 7500 AE Enschede, The Netherlands
[c] Helmholtz Centre for Infection Research and Helmholtz Institute for Pharmaceutical Research Saarland, Department of Drug Delivery, Campus A4.1, 66123 Saarbrücken, Germany
[d] University of Twente, Medical Cell BioPhysics, MIRA Institute for Biomedical Technology and Technical Medicine, P.O. Box 217, 7500 AE Enschede, The Netherlands

ARTICLE INFO

Available online 26 February 2015

Keywords:
Spontaneous Raman microscopy
Cell imaging
Drug carriers
Interaction between cell and carrier
Chemically selective visualization
Nanomaterials
Uptake
Intracellular fate of carriers

ABSTRACT

Progress in advanced therapeutic concepts requires the development of appropriate carrier systems for intracellular drug delivery. Consequently, analysis of interaction between carriers, drugs and cells as well as their uptake and intracellular fate is a current focus of research interest. In this context, Raman spectroscopy recently became an emerging analytical technique, due to its non-destructive, chemically selective and label-free working principle.

In this review, we briefly present the state-of-the-art technologies for cell visualization and drug internalization. Against this background, Raman microscopy is introduced as a versatile analytical technique. An overview of various Raman spectroscopy investigations in this field is given including interactions of cells with drug molecules, carrier systems and other nanomaterials. Further, Raman instrumentations and sample preparation methods are discussed. Finally, as the analytical limit is not reached yet, a future perspective for Raman microscopy in pharmaceutical and biomedical research on the single cell level is given.

Contents

1. Introduction

Due to the emerging knowledge about the complex processes regulating origination and course of diseases on the subcellular level, advanced therapeutic concepts have rapidly evolved over the last decade. Here, the focus for the development of novel therapeutics shifted from classical large solid dosage systems such as tablets and capsules to small so called modern drug carrier systems in micro- and nanometer size range.

☆ This review is part of the *Advanced Drug Delivery Reviews* theme issue on "Pharmaceutical applications of Raman spectroscopy — from diagnosis to therapeutics".

* Correspondence to: M. Windbergs, Saarland University, Department of Biopharmaceutics and Pharmaceutical Technology, Campus A4.1, 66123 Saarbruecken, Germany.

** Correspondence to: C. Otto, University of Twente, Medical Cell BioPhysics, MIRA Institute for Biomedical Technology and Technical Medicine, P.O. Box 217, 7500 AE Enschede, The Netherlands.

E-mail addresses: m.windbergs@mx.uni-saarland.de (M. Windbergs), c.otto@tnw.utwente.nl (C. Otto).

http://dx.doi.org/10.1016/j.addr.2015.02.006
0169-409X/

In this context, analytical investigation and evaluation of mechanisms and extent of interactions between cells and drugs became of utmost importance. Besides research on the pure drug molecule, the development of a suitable delivery system is of similar importance. So, one current scientific focus is on appropriate analysis and evaluation of interactions of drug delivery systems, their cellular uptake and the release mechanism as well as their kinetics for an incorporated drug in order to improve therapeutics as well as specific disease treatment protocols. In this respect, Raman spectroscopy as a non-invasive, chemically selective analytical technique is gaining increasing attention.

In this contribution, we aim to give a broad overview of the work that has already been performed on Raman microscopy for single cell imaging with a special focus on the interaction of cells with drugs and the uptake and intracellular fate of carrier systems for drug delivery. We start with a short introduction of eukaryotic cells as the target organisms and their endocytotic uptake mechanisms. Next, established nanocarrier systems for intracellular delivery are introduced. The section is followed by an overview of techniques suitable for cell visualization before presenting different Raman instrumentations with a summary of important instrument parameters as well as influences of sample preparation. In the following section, we present different studies on single cells by Raman spectroscopy and microscopy. Here, the important Raman bands which are characteristic for distinct molecules are discussed as a basis for visualization of cellular structures and organelles. Finally, we review the contributions in the field of drug delivery focusing on carrier uptake as well as on uptake of drug molecules. Empty and drug-loaded carriers are considered including cytotoxic aspects as well as carriers for targeted drug delivery. This review focuses on studies performed with spontaneous Raman microscopy including some investigations performed by surface enhanced Raman spectroscopy. However, for deeper insight into the field of surface enhanced Raman spectroscopy, the reader is referred to the specialized article in this issue. The same holds for readers interested in coherent Raman techniques.

1.1. Cell physiology

Eukaryotic cells have multiple compartments with different functions. The cells are confined by the plasma membrane, representing the biological barrier which molecules and potential carrier systems have to overcome to enter the cytoplasm. The cytoplasm contains the cytoskeleton, a framework of protein fibers, which mechanically stabilizes the cell and embeds different cell organelles like the nucleus and the endoplasmatic reticulum (ER). Furthermore, the cytoskeleton is important for intracellular motion such as transport of organelles and cell division as well as cell migration. The largest organelle is the nucleus, where the DNA is stored. Adjacent to the nucleus is the endoplasmic reticulum pervading the cytosol (cytoplasm without organelles) with channel like structures. The Golgi apparatus represents another closed membrane system within the cytoplasm. Here, proteins, which are synthesized in the ER, are modified. Furthermore, the Golgi apparatus plays an important role for intracellular transport of macromolecules as well as in secretion processes. Endosomes, small membrane vesicles, facilitate the transport of proteins between individual compartments of the cell and to and from the cell membrane. Organelles which are important for the cellular metabolism are mitochondria, lysosomes and peroxisomes. Mitochondria are generally referred to as cellular power plants, as they generate the chemical energy in the form of adenosine triphosphate (ATP) for the cell. Lysosomes and peroxisomes are small enzyme containing vesicles which are responsible for the breakdown of macromolecules. Especially lysosomes play an important role in the intracellular fate of pharmaceutical carrier systems and drug molecules.

1.2. Endocytosis — the major cellular uptake mechanisms for pharmaceutics

Pharmacological targets can be located outside as well as inside cells. The latter situation is attractive, however, challenging for drug therapy due to the complex cell physiology. The drug molecule has to pass numerous hurdles such as multiple biological and plasma membranes prior to reaching the target molecule within a cell. As the direct path for the molecule to the pharmacological target is long, a significant number of administered drug molecules might pursue other routes. This will decrease drug efficiency, while side effects and toxicity potentially increase. These facts have to be taken into consideration when developing novel therapeutics.

Generally, the hydrophobic plasma membranes are an insurmountable obstacle for the majority of therapeutic molecules. Only molecules such as steroids/hormones, liposoluble vitamins, water, amino acids and glucose can passively be transported across the hydrophobic membrane along their concentration gradient. Other molecules are actively transported by specific carrier proteins even against a concentration gradient at the expense of ATP. Besides carrier proteins, endocytosis is the major route for the internalization of extracellular substances into the cell body through the formation of vesicles. Various nanocarriers have already been introduced to transport drug molecules into cells and release their cargo intracellularly, close to the target structures.

Depending on the cell nature and the physicochemical characteristics of the nanocarrier, the major internalization pathways are phagocytosis and other endocytic pathways (Fig. 1). Macrophages, monocytes, neutrophils and dendritic cells are specialized phagocytic cells (so called professional phagocytes) [1]. In comparison, non-professional phagocytes including cell types such as fibroblasts and epithelial as well as endothelial cells perform phagocytic activity to a lower extent [3]. Internalization by phagocytosis generally comprises of three steps. First, nanocarriers are recognized in the bloodstream by opsonization. Second, opsonized particles adhere to the cell, before subsequent ingestion is taking place.

Non-phagocytic endocytosis (also referred to as pinocytosis) is a process happening in all other cells. These non-phagocytic pathways can be divided into clathrin-mediated endocytosis, caveolae-mediated endocytosis, macropinocytosis as well as other clathrin- and caveolae-independent endocytosis (Fig. 1).

Clathrin-mediated endocytosis, as the predominant mechanism in most cells, can occur receptor-dependent and receptor-independent via the formation of clathrin-coated vesicles in clathrin-rich membrane regions of the cell. The protein clathrin forms triskelia [2] which assemble in a lattice on the cytosolic surface of the cell membrane. This process facilitates the deformation of the membrane into a coated pit, which is continuously invaginated as the clathrin lattice formation proceeds, until the clathrin-coated vesicle is fissioned.

Caveolae, flask-shaped cell membrane invaginations lined by the protein caveolin along with cholesterol and sphingolipids, can also mediate endocytosis. They occur in substantial numbers in endothelial cells, composing 10–20% of the cell surface [4]. Similar to clathrin-mediated endocytosis, the GTPase dynamin mediates the fission of the caveolae with the particle from the membrane, thus forming a cytosolic caveolar vesicle.

Macropinocytosis happens through the formation of actin-driven cell membrane protrusions. In contrast to phagocytosis, the protrusions collapse and subsequently fuse with the plasma membrane instead of zipping up the ligand-coated particle [4].

As eukaryotic cells are 10–50 μm in size, potential carrier systems have to be of appropriate size to be internalized. It was shown that model polystyrene particles have an ideal phagocytosis rate in vitro for sizes ranging from 250 nm to 3 μm [5], whereas vesicles formed by non-phagocytic mechanisms are sized from 50 nm up to more than 1 μm [4,6–8].

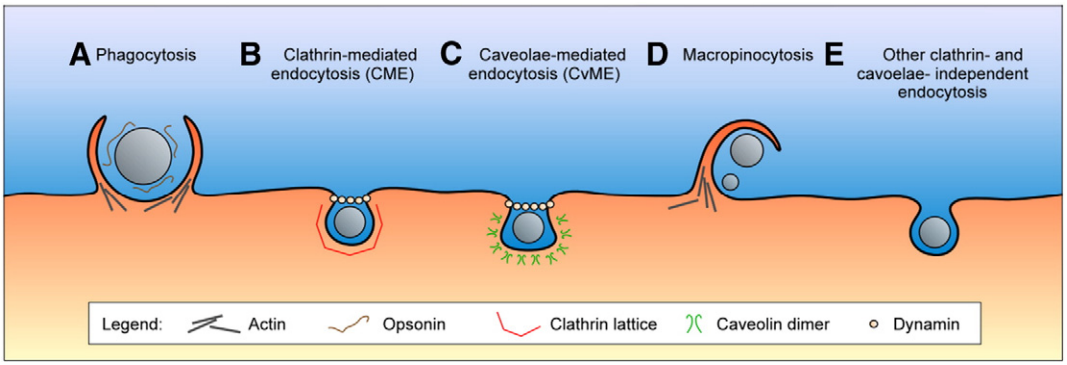

Fig. 1. Principal nanocarrier internalization pathways in mammalian cells. **A** Phagocytosis is an actin-based mechanism occurring primarily in professional phagocytes, such as macrophages, and closely associated with opsonization. **B** Clathrin-mediated endocytosis is a widely shared pathway of nanoparticle internalization, associated with the formation of a clathrin lattice and depending on the GTPase dynamin. **C** Caveolae-mediated endocytosis occurs in typical flask-shaped invaginations of the membrane coated with caveolin dimers, also depending on dynamin. **D** Macropinocytosis is an actin-based pathway, engulfing nanoparticles and the extracellular milieu with a poor selectivity. **E** Other endocytosis pathways can be involved in the nanoparticle internalization, independent of both clathrin and caveolae. Figure and caption taken from reference [2] (Fig. 2) — "With kind permission from Springer Science and Business Media".

Different nanocarriers including polymeric, lipid and complex nanoparticles as well as diverse vesicles have been developed for intracellular drug therapy. Nanocarriers are actively internalized through endocytosis and can release their drug inside the cell. Almost any cell type is able to take up particles via an endocytotic pathway. However, the extent differs from cell type to cell type. By varying raw material, size, shape, charge and surface structures of nanocarriers, the pathway and extent of uptake, as well as the fate of carrier and drug inside the cell may be influenced.

For further detailed reading on endocytotic mechanisms as well as the dependence of physico-chemical characteristics of the nanocarriers on cellular internalization, the reader is referred to Hillaireau et al. [2].

1.3. Drug delivery systems for cellular applications

In the pharmaceutical context, nanoparticles are defined as solid colloidal particles in the size range of 10–1000 nm [9]. Polymeric nanoparticles are made of synthetic biodegradable polymers such as poly(lactic acid) (PLA) and poly(lactic-co-glycolid acid) (PLGA) or natural polymers such as albumin and chitosan [2,10]. The polymers should be biodegradable as well as non-toxic and non-immunogenic [10,11]. The latter two are also required for the degradation products of the original polymer. Polymeric nanoparticles are subcategorized into nanocapsules and nanospheres. Nanospheres are solid matrix particles, whereas nanocapsules are vesicular systems with a core shell structure. The liquid or semisolid core is embedded in a solid shell. Drugs can be embedded inside or adsorbed on the nanoparticle. Different fabrication techniques are described in detail elsewhere [10].

Further polymer therapeutics include simple polymer drug conjugates, micelles, dendrimers and polyplexes [12,13].

Micelles are self-assembling colloidal aggregates of amphiphilic block-copolymers, entrapping the drug [12,14]. Polyelectrolyte complexes known as polyplexes are formed by electrostatic interactions of polycations and nucleic acids [2,12]. Dendrimers have a three-dimensional architecture, where a macromolecule contains symmetrically arranged braches [12].

Liposomes are artificial spherical vesicles composed of phospholipid bilayers [15]. Biocompatibility, biodegradability as well as low toxicity and immunogenicity are only a few felicitous attributes which have made liposomes an attractive drug carrier system. Due to the aqueous core surrounded by a phospholipid bilayer, both hydrophobic and hydrophilic molecules can be incorporated. Furthermore, liposomes can be functionalized in many ways and are widely addressed in literature [15].

Many more nanocarrier systems have been introduced in pharmaceutical sciences. Here however, we only want to give a brief introduction about the nanocarrier systems which are utilized in the manifold studies described hereafter.

1.4. State-of-the-art techniques for cell visualization

Cells can be visualized with many different techniques. The most general analytical procedure is light microscopy, which is routinely used in every cell culture lab. It offers a quick evaluation of cultured cells with respect to morphology and confluence levels. However, this visual examination is not sufficient or suited for specialized investigations, due to the lack of meaningful molecule specific information that can be related to detailed structural information of cells.

Other techniques like electron microscopy and atomic force microscopy are also utilized for cell visualization. Both techniques are capable to resolve subcellular structures. However, due to their working principles, images can only be recorded from surfaces, meaning that interior structures require destructive sectioning of the sample prior to analysis. Furthermore, the recorded images are not based on chemically selective detection of sample structures, hindering analytical distinction between carrier systems and cell compounds for example. To circumvent these issues and to benefit from the high resolution of electron and atomic force microscopy, so called correlative microscopy has been established, where two complementary imaging techniques are combined. In most cases, confocal fluorescence microscopy is used as the current state-of-the-art technique for cell visualization.

In fluorescence microscopy, chemically selective visualization of different structures of the cell is accomplished by the introduction of external fluorescent marker molecules which specifically bind to the structures of interest. Due to the wide application of this spectroscopic technique, numerous marker molecules have been introduced to visualize any subcellular structures. However, the number of structures which can simultaneously be imaged is limited, as each marker molecule is excited by one distinct wavelength during analysis. In spite of this limitation, confocal laser scanning fluorescence microscopy (CLSM) is an established technique for visualizing interactions, cellular uptake and fate of nanocarriers within cells. Herd et al. [16] for example used CLSM to study the influence of different geometries and surface orientation of FITC labeled silica nanoparticles on cellular uptake, whereas Torchilin et al. [17] followed the targeting of liposomes and micelles to cells as well as their intracellular fate by fluorescence microscopy. Despite its wide application, this technique bears several disadvantages. Due to the artificial labeling of the drug molecule or a carrier component, the physico-chemical characteristics of the analyzed system are altered, potentially leading to different uptake patterns and changing

their internal fate. If the fluorophor is not sufficiently bound to the carrier and disassembles, it might possibly attach to other structures of the sample. Furthermore, the susceptibility of many marker molecules to photo-bleaching confounds fluorescence microscopy analysis over longer time spans, thus hindering investigations of carrier and drug fate inside the cell. There is a need for techniques that enable chemically selective analysis to visualize and gain knowledge about uptake, localization and fate of drug carrier systems and their loadings over sufficiently long time scales. Here, vibrational microspectroscopy such as infrared (IR) absorption spectroscopy and imaging, spontaneous Raman spectroscopy and imaging as well as coherent Raman techniques are interesting alternatives. Vibrational microspectroscopy is based on the detection of molecular vibrations arising from functional groups within the sample and does not require compound labeling. Therefore, IR absorption spectroscopy and Raman spectroscopy are attractive techniques for non-destructive and label-free imaging, while maintaining chemical selectivity. Furthermore, both techniques can be combined with optical microscopy enabling powerful approaches for non-invasive chemical imaging. IR microspectroscopy has successfully been applied to image for instance sarcoma and HeLa cells [3,18], also in direct comparison to Raman images [18]. Due to the superior resolution of Raman microscopy (<1 μm) compared to IR microscopy (~10 μm) and its applicability in aqueous environments, confocal Raman microscopy is today the prevalent technique for cellular visualization. In contrast to the analysis of light absorption (IR), light scattering is detected in Raman spectroscopy. The so called Raman effect was first reported by the Indian physicist Sir Chandrasekhara Venkata Raman in 1928 [19] and is a rather weak effect compared to light absorbance or reflection. The major fraction of photons is scattered at the same wavelength as the incident photons (Rayleigh scattering). A smaller number of photons shift in frequency (or wavelength), which is referred to as Raman scattering. This inelastically scattered light carries information of the vibration of atoms in a molecule, which are typical for each chemical moiety. If the Raman scattering has a lower energy than the incident photon (e.g. longer wavelength), it is referred to as Stokes scattering, whereas the opposite process, where the scattered light has a higher frequency (e.g. shorter wavelength), is called anti-Stokes scattering. The specific wavelength shift between incident and scattered photon represents a unique feature of a specific chemical structure and is therefore referred to as a molecular fingerprint.

2. Sample and instrumental prerequisites for spontaneous Raman imaging of cells

Raman imaging is based on collecting spatially resolved data. This is achieved by coupling a Raman spectrometer with a confocal optical microscope. A first self-built confocal Raman microspectrometer with a resolution of ≤1 μm^3 was described in 1990 [20]. However, immense technical progress led to an increased accessibility and a variety of commercially available instruments over the last years. In general, confocal Raman microscopes are assembled of a few building blocks. The center piece is an optical microscope with a pinhole enabling confocal detection. A laser source is coupled to the microscope irradiating the sample, which is placed on the scan stage of the microscope, through an objective. The scattered light from the sample is collected, passes through the pinhole and is subsequently directed into a spectrometer. The spectrometer and the attached camera comprise the detection unit for spectral collection. Signals from out of focus points are rejected by the pinhole. Thus, background signals are strongly reduced and depth resolution is provided.

An important instrumental parameter is the choice of a suitable laser source for Raman imaging depending on factors like wavelength and laser power. Shorter wavelengths generate higher numbers of scattering photons, thus, increasing the scattering efficiency and therefore Raman intensity of the weakly scattering biological samples. However, shorter wavelengths typically provoke more autofluorescence from the sample, potentially exceeding the Raman signal. Hamada et al. [21] compared the autofluorescence background signal from cells for 488, 514 and 532 nm excitation concluding that the 532 nm excitation compromises best between autofluorescence and Raman signal intensity for live cell imaging. Furthermore, photodamage, which is caused by light absorption of a biological sample, has to be considered upon choosing an adequate laser source. Cell damage decreases at longer excitation wavelength. This was demonstrated by Puppels et al. [22] and by Notingher et al. [23] studying the spectral consequences of irradiating living cells with different laser lights, namely 660 and 514.5 nm, as well as 785, 514 and 488 nm, respectively. Unfortunately, a strong decrease in Raman scattering intensity goes along with an increase in wavelength [24]. Thus, high Raman scattering efficiency and low photodamage are two contrary parameters to be negotiated prior to analysis. Therefore, an excitation wavelength of 785 nm is a good compromise, as signal strength is reasonably high, whereas fluorescence and cell damage are low. For similar reasons, this wavelength is often used in Raman studies analyzing tissue especially skin. Additionally, light from the near infrared region penetrates sufficiently deep into tissue. Although cell damage continuously decreases at longer wavelength, lasers with an excitation wavelength of 1064 nm are inappropriate for spontaneous Raman spectroscopy due to inefficient Raman scattering [24].

Raman imaging can benefit tremendously from biomolecules showing a resonance Raman effect. This effect can be triggered by utilizing a laser wavelength close to or on the absorption band of the molecule resulting in strong Raman scattering. Thus, it can be exploited to image for example the molecular distribution of cytochrome c located in the mitochondria of cells, as this electron carrying molecule gives rise to a strong resonance Raman effect at 532 nm [25].

An important factor for cell imaging is the resolution of the image to capture the subcellular structures in the lower micrometer and nanometer size range as well as the nanocarriers. The lateral resolution is determined by the numerical aperture of the objective in combination with the wavelength of the laser light, whereas the axial resolution is also influenced by the pinhole and the refractive index of the immersion medium [26]. With the currently available Raman instruments, a lateral resolution down to 200 nm and an axial resolution of 500 nm can be achieved, making the technique feasible for visualization of subcellular structures and drug carriers.

Despite few exemptions, cells are commonly cultured submerse in aqueous medium. However, the aqueous environment does not impede Raman microscopy analysis. As Raman spectroscopy is based on the polarization of molecules, water molecules contribute less pronounced peak patterns in the spectrum than in IR absorption spectroscopy for example. Furthermore, the water bands arise in regions of the spectrum where other groups give no or minor contributions. Therefore, the Raman scattering of water hardly interferes with other spectral bands during analysis. Air or immersion objectives are used when working with an inverted microscope. The use of upright instruments is not adverse as water dipping objectives are available for application. Although aqueous environments do not generally interfere with data acquisition, attention has to be drawn to supplements such as nutrients or colored indicators in the cell culture medium, as they can contribute disturbing background signals. For example, the pH indicator phenol red which is a standard supplement in cell culture media as it facilitates an immediate visual evaluation of the medium, shows a fluorescence signal. Thus, available phenol red free medium should be used for Raman imaging.

The low Raman spectral cross-section of biological samples necessitates the consideration of the correct sample substrate. The cells need to grow on the substrates surface. In addition, the substrate should show a very low background signal. Thus, standard plastic substrates are inapplicable for Raman microscopy as their background signal masks the Raman signal from the cell sample. In order for the excitation light to get to the sample with minimum loss, the substrate should be

transparent to the near-infrared and visible region of the light spectrum. A study by Draux et al. [27] shows the influence of diverse substrates (plastic, quartz, calcium fluoride (CaF_2) and zinc selenide (ZnSe)) on cell morphology, proliferation and substrate eligibility for Raman spectroscopy. While ZnSe was discarded due to cell toxicity, and plastic was withdrawn due to its high background signal, detailed Raman spectra were obtained from cells grown on quartz and CaF_2 substrates. Thus, due to their low background signal, calcium fluoride and quartz should be used for Raman imaging of cells [25,28].

Spatially resolved spectral data sets can be acquired in two ways in confocal Raman microscopy. Either the laser is scanned back and forth across the sample which is in a fixed position, or the sample is positioned on a motorized microscopic stage and constantly moved through the laser beam. In both cases, a Raman spectrum is recorded at every preselected position retrieving a spatially resolved data set. Cells which grow attached to surfaces are automatically immobilized for analysis and do not hinder the acquisition of spatially resolved spectra. However, cells growing in suspension (such as blood cells) are more challenging for spectral analysis. Here, optical tweezers for cell trapping, and thus customized immobilization have been combined with Raman spectroscopy [29,30]. In laser tweezers Raman spectroscopy (LTRS), the simultaneous analysis of living cells over longer time periods under the same environmental conditions is basically impossible due to weak Raman scattering activity of the cell sample and resulting long acquisition times. Multifocal LTRS was introduced for parallel acquisition of Raman spectra from suspension cells [31]. However, the detection of spectral signals was only possible in a 1-D scheme. Kong and Chan [32] improved the analytical capabilities of LTRS by developing a modulated multifocal detection scheme. Due to the introduction of a spatial light modulator, multiple cells can be trapped in the generated holographic laser tweezers in a 2-D array. Raman spectra from this 2-D array of samples are then collected in parallel from different combinations of multifocal patterns by the spectrometer of the implemented multifocal detection scheme. Creely et al. [33] have demonstrated holographic optical tweezers (HOT) for Raman imaging of floating Jurkat cells. The individual cell is immobilized in the multiple trapping site of the HOT and guided back and forth across the focus of the stationary Raman laser excitation beam, thus building up a cell image.

As conventional confocal Raman microspectroscopy is still rather slow in recording a spectral data set due to high resolution stepwise sample rasterization and acquisition times, Okuno and Hamaguchi [34] developed a multifocus system for fast multimode vibrational imaging as a potential tool for *in vivo* applications and real time studies of living cells. Another multifoci-scan confocal Raman microscope was developed by implementing galvano mirrors into the laser light pathway [35]. The laser beam is raster scanned across the sample by a pair of galvano mirrors generating multifoci excitation. Excited Raman scattering is simultaneously projected onto a multichannel spectrograph by a third galvano mirror. Overall, image acquisition time was significantly reduced while diffraction-limited resolution was retained. Thus, it became possible to monitor fundamental processes in cells occurring within one minute.

A variety of fixation methods including formalin, methanol, air-drying and cytocentrifugation are available to preserve cell samples for later or prolonged analysis. However, fixation might change spectral information, when compared to Raman spectra from live cells. Draux et al. [36] investigated the influence of cell fixation on spectral changes in Calu-1 cells. Raman spectra were related to spectra acquired from extracted cell structures and live cells. It was shown that 4% formalin-fixation and cytocentrifugation keep cells in a similar state to their living form. However, any method including air-drying caused spectral deviations. The suitability of formalin-fixation was also shown by Chan et al. [37]. Methanol fixation caused delineation between normal and leukemia cells, whereas data misclassification was not shown for spectra derived from formalin fixed cells. Konorov et al. [38] presented a spectral comparison based on Raman spectroscopy between live and dry-fixed human embryonic stem cells (hESC) in their undifferentiated and differentiated form. The rapid increase in intensity ratios (757 cm^{-1} to 784 cm^{-1}) of Raman bands assigned to the tryptophan ring breathing mode in proteins and to nucleic acid backbone and pyrimidine base vibrations can be correlated with cell differentiation. This trend was also observed when comparing peak ratios obtained from live and dry-fixed stem cells at different time points of differentiation. Excellent agreement ($p < 0.0001$) was found between ratios measured before and after dry fixation. Thus, dry-fixed stem cells are a valuable substitute for living cell samples for time consuming Raman mapping applications as temporal spectral patterns of differentiation are preserved. A study by Mariani et al. [39] revealed that the influence of the fixation method is also depending on the chosen cell line. By probing breast and colorectal circulating tumor cells in comparison to human normal lymphocytes, Raman spectra of dried out samples were best to be discriminated from each other using principal component analysis than spectra derived after methanol or paraformaldehyd fixation [40].

After successful acquisition of a spectral data set from the sample, the raw data have to be processed in order to detect individual compounds of the sample, and based on their molecular fingerprint generate a false color Raman image. The first processing step usually referred to as pre-processing includes the removal of cosmic ray artifacts from the data set as well as the reduction of background noise to receive spectra with a smooth baseline. The pre-processed spectral data set is then further processed by means of multivariate data analysis procedures. In this step, false color images are generated by mapping the scores or parameters yielded for each Raman spectrum of the data set by a multivariate method as a function of spatial coordinates. In general, this comprises two complementary approaches. Either the data set is clustered according to similarities of the spectra or spectral unmixing algorithms sort the data according to their greatest dissimilarities. Lasch [41], Hedegaard et al. [42], and Miljković et al. [43] discussed methods for spectral pre-processing and algorithms for multivariate data analysis, respectively, in detail. For further insight on handling Raman spectral data sets, the reader is also referred to the respective article in this issue, as this subject is beyond the content of this article.

3. Studies on single cell imaging

The major building block molecules of a cell comprise proteins, nucleic acids, lipids as well as phospholipids, and carbohydrates among others. Molecular vibrations deriving from the functional groups of these building blocks define the Raman spectrum of cells.

A Raman spectrum can be divided into three parts: the fingerprint region <1800 cm^{-1}, the silent region 1800–2800 cm^{-1} and the high frequency region >2800 cm^{-1} [44].

The molecular fingerprints of the functional groups can be found below 1800 cm^{-1} and above 2800 cm^{-1}, which is dominated by CH-stretch vibrations. Cellular Raman spectra have intensively been investigated in numerous studies. Thus, characteristic Raman bands could be assigned to functional groups of building block molecules. As an example, Raman spectra of the main molecules present in cells proteins, nucleic acids, and lipids are shown in Fig. 2. Furthermore, an overview about important band positions and cell related functional groups is given in Table 1. Listed wavenumbers may vary, as the given peak position is directly related to the resolution of the used spectrometer. For further band assignments, the reader is referred to the cited literature. In the silent region, no natural molecular vibrations of cells occur. Thus, molecules with distinct Raman signals in this region can clearly be distinguished from cell spectra. This beneficial trick was used in several studies and allowed liposome tracking within cells or the supervision of cell division. These studies and the exploitation of specific molecular bonds such as alkyne and carbon–deuterium are further discussed below.

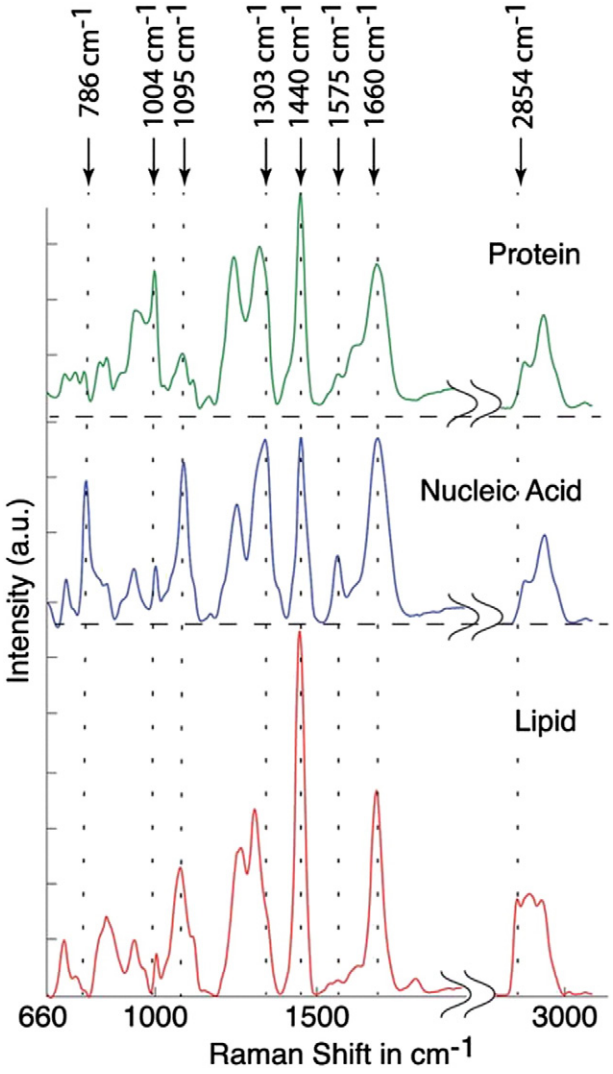

Fig. 2. Raman spectra of important cellular molecules protein, nucleic acid and lipid. Adapted from reference [54] with permission of The Royal Society of Chemistry.

Puppels et al. [20] were the pioneers in introducing confocal Raman microspectroscopy studying single cells and chromosomes. They discussed Raman lines of spectra recorded from the cytoplasmic region and the nuclei of human eosinophilic granulocytes. For a better understanding of banding patterns, Raman analysis of metaphase chromosomes was carried out as well.

Differentiation of murine embryotic stem cells was studied by Notingher et al. [55,56]. The state of mRNA translation was monitored by the ratio between RNA and protein peak areas (813 and 1005 cm^{-1}, respectively). Furthermore, the intensities of RNA (813 cm^{-1}) and DNA (786 cm^{-1}) derived Raman peaks were identified as *in vitro* differentiation markers. The decrease in RNA peak suggest the usage of RNA for protein synthesis during early cell differentiation stages, whereas a lower intensity of the DNA peak indicates a reduced proliferation rate of the cells upon development of a mature phenotype. Results from Chan et al. [57] go along with the latter observation. They also reported an intensity decrease of the DNA and RNA peaks (785, 1090 and 811 cm^{-1}, respectively) during differentiation of human embryonic stem cells into cardiomyocytes. The study was based on averaged single point Raman spectra. The cellular location from which these data were taken was not based on Raman spectroscopy. Here, the work of Zuser et al. [58] commenced. They imaged murine embryonic stem cell colonies with confocal Raman microspectroscopy. By applying vertex component analysis (VCA) and hierarchical cluster analysis, they reconstructed false color images showing biochemical compartments within the cell colonies: the nuclei surrounded by cytoplasm embedded in the extracellular matrix with lipid/phospholipid inclusions. The chosen multivariate methods for image reconstruction are complementary. VCA is an unsupervised spectral unmixing algorithm, decomposing each spectrum of the hyperspectral data set (data matrix) into a linear combination of the pure component spectra (so called endmember spectra) [42,43], whereas hierarchical cluster analysis tries to find spectral similarities. The algorithm continuously searches for the most similar spectra, groups them and recalculates repeatedly until all spectra are combined into a small number of clusters [42,43].

Further work on human embryonic stem cells with regards to label-free determination of the cell cycle phase *in situ* was performed by Konorov et al. [59]. By integrating the DNA band intensity (783 cm^{-1}) across individual cell nuclei, the plotted histogram displayed a profile nicely corresponding to fluorescence intensities in flow cytometry. Thus, based on DNA band intensities which were corrected for RNA content using the RNA band at 811 cm^{-1} the stem cells could be assigned to the different cell cycle phases gap phase (G1), DNA replication phase (S), or gap phase/mitosis (G2/M).

Periodic passaging is a standard procedure in maintaining cells in culture. However, cell detachment from the substrate and re-plating at a lower cell concentration is a major perturbing factor for the cultured cells and may lead to variances in their Raman spectra. To confine spectral changes in Raman signatures due to subcultivation from changes occurring during cell differentiation, Konorov et al. [60] performed a study on human embryonic stem cells (hESC). Minor differences were noticed in the mean intensities of the Raman signatures of hESC, the variances of certain peaks changed markedly and maximized 48 h after passaging. The peak at 480 cm^{-1}, which is associated with glycogen, was identified as the major contributor to the spectral variations. A false color Raman image of glycogen distribution in a hESC colony was congruent with periodic acid Schiff staining of glycogen of the same colony area. Subsequently, the authors developed a procedure for absolute quantification of intracellular glycogen content in the same cell type by Raman microspectroscopy [61]. Sample placement within the collective volume for spectral acquisition and transparency as well as low elastic

Table 1
Assignment of Raman band positions dominant in cell spectra.[a]

Band position [cm^{-1}]	Assignment		
785–788	Pyrimidine bases	Ring breathing	Nucleic acids
1002–1005	Phenylalanine	Symmetric stretch	Proteins
1092–1095	O–P–O	Symmetric stretch	Nucleic acid backbone, phospholipids
1254–1255	Amide III	CH/NH deformation	Proteins
1425–1475	CH_2, CH_3	Deformation	Proteins, lipids
1655–1662	Amide I	C = O stretching mode	Proteins
2800–3020	CH_3, CH_2, CH	Stretching	Lipids, proteins, other

[a] Band assignments according to references [45–53].

scattering efficiency of sample and calibration reference are the two conditions proposed in order to gain a linear proportion between Raman signal from the sample and the amount of analyte in the sample. The introduced method was validated against glycogen quantification with a commercially available glycogen assay kit.

Another spectroscopic study was presented by Tan et al. [62] underlying the value of Raman microspectroscopy for stem cell research. Here, the authors compare spectral features of human induced pluripotent stem cells (hiPSC), human embryonic stem cells as well as non-specifically differentiated progeny of human embryonic stem cells. Reprogramming seemed to lead to a reduced protein to nucleic acid ratio, thus, hiPSC were spectroscopically similar to human embryonic stem cells, however clearly distinguishable from differentiated human embryonic stem cells. Nevertheless, the authors state that although the obtained spectroscopic results are quite intriguing, further investigations are absolutely necessary to exclude potential cell line artifacts.

During apoptosis, changes in DNA, proteins, and lipids occur. As a result of cleavage, the DNA double strand is chopped in multiple fragments, proteins are broken down, while lipid vesicles are formed. These molecular changes were observed spectroscopically by inducing cell death of A549 cells (human lung carcinoma epithelial cells) with Triton X-100 [4]. Cell viability and DNA integrity were tested with standard method for comparison.

Despite the common approach to recognize cell death by spectral changes in the fingerprint region, Caponi et al. [63] followed changes in the CH-stretch region at around 3000 cm^{-1} in the Raman spectrum. In particular, vibrational modes of membrane lipids assigned to peaks at 2854 cm^{-1} and 2874 cm^{-1} [64,65] were investigated in Jurkat cells for different hydration states using band shape analysis.

Intracellular hydrodynamics were suggested as another biomarker for the indication of cell functions. Based on nonlinear coherent anti-Stokes Raman scattering microscopy studies by Potma et al. [66] showing a clear separation of intracellular water domains from the extracellular environment, Fukunaga et al. [67] monitored the time-dependent water concentration changes in human acute promyelocytic leukemia cells (HL-60) and imaged cells at high and low water concentrations using spontaneous Raman microspectroscopy. Label-free images were constructed based on Raman bands of proteins (1650 cm^{-1}), lipids (2940 cm^{-1}) and water (3400 cm^{-1}).

Up to here, only studies were discussed which are based on the acquisition of single Raman spectra. Single Raman spectra give spectral and therefore chemical information about distinct sample positions, whereas Raman imaging provides the chemical information paired with spatial information. Thus, the focus shifts towards Raman imaging of entire cells and their subcellular structures in the following passage.

The difference between spectral information obtained by acquiring single point Raman spectra in comparison to full hyperspectral Raman information of the entire cell was shown by Chan and colleagues [54,68]. The group investigated doxorubicin-induced changes in Jurkat T cells representing a model system of T-cell leukemia recording single Raman spectra as well as images of the entire cell with different instrumental approaches. In a first study, laser tweezers Raman spectroscopy (LTRS) was applied to gain point spectra of optically trapped suspension cells during exposure to doxorubicin over different time periods [68]. The observed sequence of spectral changes was consistent with different stages of drug-induced apoptosis including vesicle formation, cell membrane blebbing and chromatine condensation. After an increase in lipid peaks (1266, 1303, 1445, 1656, and 1740 cm^{-1}), an intensity increase in DNA Raman peaks (785, 1092, 1340, and 1578 cm^{-1}) was detected followed by changes in DNA (signal decrease of peaks at 785, 1092, 1340, and 1578 cm^{-1}) and protein Raman vibrations (increase of phenylalanine band at 1004 cm^{-1}). Thus, the authors concluded that LTRS is a valuable technique for real-time monitoring of biochemical changes of suspension cells *in vitro*. However, the single Raman spectrum recorded from a fraction of the entire cell volume in point spectroscopy is generally taken as a representative signature of the whole cell. Therefore, a subsequent study by the same group used the same model of doxorubicin treated Jurkat T cells and investigated drug induced changes by line-scan Raman microspectroscopy gaining global spectral information of each cell [54]. It was shown that locally and globally acquired Raman spectra of nucleic acids, proteins, and fatty acids show a different behavior as a function of drug exposure time due to an inhomogeneous distribution of the molecular content of a cell. Therefore, in this case the discrimination of doxorubicin exposed and control cells based on local information of protein content gathered by point spectroscopy would have been very difficult, whereas groups of cells were successfully separated based on the significant spectral differences from the global cellular level (line-scan Raman microspectroscopy).

Uzunbajakava [28] presented Raman imaging of protein distribution in cell types with differing levels of transcription. Peripheral blood lymphocytes as maturated cells exhibiting a low level of nuclear transcription show a varying nuclear distribution of proteins, whereas epithelial cells have a more homogenous protein distribution over the nuclear space. The DNA intensity has on average been lower within the nucleus in this cell type, as dynamic processes such as transcription and replication were constantly in progress. Different protein distribution in the two cells types was shown in lateral Raman images made at a high frequency protein band at 2850, 2885, and 2935 cm^{-1}. Subsequently derived profiles through the protein images illustrated the protein variations in a cross section plot. It was further shown, that protein distribution was identical for images obtained from the high frequency bands (2800–3030 cm^{-1}) and from the low frequency bands (1433–1481 cm^{-1}) [69]. However, care has to be taken when analyzing a protein/lipid system due to the overlap of the band derived from the phospholipid vesicle and the peak for protein image reconstructions at 1440 and 1451 cm^{-1}, respectively. Protein and DNA distribution was also shown in Raman images of apoptotic HeLa cells [69]. DNA was fragmented in later stages of taxol initialized apoptosis. Line profiles through Raman images reconstructed in the 788 cm^{-1} band showed locally high intensity areas, where the DNA fragments are situated. Here, the DNA signal intensity was ~4–5 fold higher than in healthy HeLa cells.

Krafft et al. [64,70] mapped single cells such as fibroblasts and their subcellular structures. Raman bands in individual spectra were first assigned to nucleic acids (DNA and RNA), cholesterol and phospholipids as well as to proteins. Then, false color maps were constructed by multivariate approaches, which were shown to be superior to univariate methods due to resolving band overlaps of cell constituents. Furthermore, lung fibroblasts were imaged in anaphase, after mitosis and in normal cell medium (Fig. 3) [71]. The location of nucleus and vesicles within the cytoplasma and the appearance of microtubules were presented in false color maps. Changes of organelles and cell morphology upon induced stress (adding of glyoxal) and into the apoptotic stage were displayed in comparison to healthy cell states. Changes in Raman spectra of nucleus and cytoplasm were monitored along and important band changes related to the cell state were discussed.

Similar to Krafft et al., Matthäus et al. [49] reported on the advantageous use of multivariate image reconstruction algorithms over univariate methods for generating false color maps from Raman hyperspectral data sets. Here, fixed HeLa cells could be visualized in detail depending on the different biochemical composition of cell structures with a major focus on mitochondria (Fig. 4). Mitochondria are involved in ATP synthesis and consist of a complex membrane structure located inside the cytoplasm. Clustered Raman spectra from the perinuclear region showed a more pronounced peak around 2850–2900 cm^{-1} in the shoulder of the CH-stretch bands, arising from the alkane chains of lipids. Another difference to nuclei spectra was the presence of a peak at 715 cm^{-1}, which potentially originated from the choline group of phospholipids abundant in membranes. Mitochondria rich areas in pseudo color Raman maps of HeLa cells (Fig. 4 D–F) are congruent with

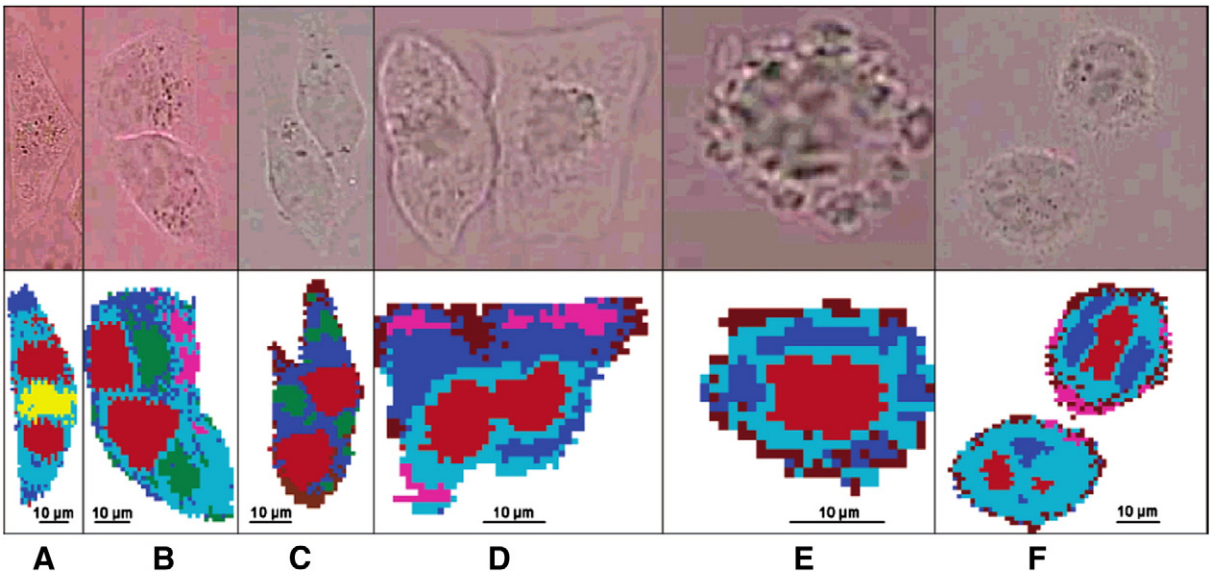

Fig. 3. Light microscopy images (top row) and corresponding Raman maps of lung fibroblast cells (bottom row) in different cell live stages. Cell after mitosis (A) and under standard cultivation conditions (B, C). Cells after stress induction (D, E) and in apoptosis (F). Colors are assigned to different cluster memberships of the Raman spectra of nucleus (red), cytoplasm (blue, cyan), microtubule (yellow), vesicles (green), peripheral membrane (brown), and inclusion bodies (magenta). Reprinted with permission from reference [71]. Copyright (2006) American Chemical Society.

fluorescence images of the same sample (Fig. 4 A–C), where the mitochondria were stained with mitotracker.

The formation of lipid droplets in cells has extensively been investigated, as the cellular lipid cycle has an impact on arteriosclerosis due to foam cell formation, liver diseases or cancer cells. The formation of lipid bodies in neutrophils was observed after cells were exposed to arachidonic acid for 1 h, where unstimulated neutrophils did not contain lipid bodies (Fig. 5) [44]. Lipid bodies were clustered as high punctuate regions comprising strong Raman peaks derived from unsaturated moieties at 1658, 1267 as well as 1441 cm^{-1} for CH_2 deformation (Fig. 5 C, D). Furthermore, it was demonstrated that lipid bodies reassemble around ingested polystyrene beads. To confirm the origin of lipid bodies due to the exposure of arachidonic acid, Raman analyses were repeated using deuterated arachidonic acid (Fig. 5 E–G). As a consequence of proton substitution, the vinylic =C–H stretch vibrations shift from 3013 cm^{-1} to 2220 and 2249 cm^{-1} (Fig. 5 H). As the vinylic =C–D stretch vibrations are located in the silent region of the cellular Raman spectrum, no other bands were interfering and the presence of arachidonic acid was visualized anywhere in the cell body. The obtained images using deuterated arachidonic acid are congruent with previous results. Furthermore, the appearance of a Raman band at 1740 cm^{-1} in the spectrum of the lipid body representing carboxyl ester C = O stretch vibration gives evidence that arachidonic acid is partially esterified in lipid bodies.

Majzner et al. [72] imaged the formation of lipid droplets in aortic endothelia cells after supplying arachidonic acid. Their size and distribution was displayed in three dimensions inside the cytosol with respect to nuclei. Dominant peaks in the Raman spectrum of lipid droplets can be assigned to unsaturated fatty acids namely oleic and arachidonic acid, giving information about the biochemical composition of lipid droplets in cells. Stiebing et al. [73] studied the uptake of arachidonic acid in human macrophages (THP-1). The exogenously fed polyunsaturated fatty acid was deuterium-labeled and therefore, distinguishable from intracellular lipids. Raman images showed uptake and storage in lipid droplets over time. However, storage efficiency and foam cell formation due to a lipid overload was more pronounced, when macrophages were provided with extracellular deuterated palmitic acid.

The excessive presence of lipid droplets in colorectal cancer stem cells (CR-CSCs) in comparison to differentiated colon cancer cells and normal colon epithelial cells was shown by Tirinato et al. [74]. Both peaks at 1300 and 2850 cm^{-1} related to lipid vibrations were space-correlated in Raman images and showed the highest intensity in CR-CSCs. Results were confirmed by measuring lipid droplet expression with flow cytometry. Furthermore, the lipid droplet content was correlated to an over-expression of known markers for CR-CSCs.

An abnormal accumulation of esterified cholesterol in lipid droplets of prostate cancer tissue was reported by Yue et al. [75]. In a first step, intracellular lipid droplets were visualized by coherent anti-Stokes Raman imaging proving that morphologically identical information was obtained in comparison to classic hematoxylin and eosin staining. In order to evaluate the lipid composition, confocal Raman spectral analysis was utilized. In normal prostate, the characteristic C = O ester stretching band at 1742 cm^{-1} was absent suggesting that stored lipids were primarily unesterified. Contrarily, spectra of intracellular lipid droplets in prostate cancer were almost identical to the spectrum of pure cholesteryl oleate showing bands at 428, 538, 614, and 702 cm^{-1} for cholesterol rings as well as the ester bond. On the basis of a calibration curve using the height ratio of the 702 cm^{-1} band and the 1442 cm^{-1} band (CH_2 bending) of spectra recorded from mixtures of cholesteryl ester and glyceryl trioleate, the cholesteryl ester percentage in lipid droplets of prostate cancer was quantified. Results were confirmed by electrospray ionization mass spectrometry, and thus the authors concluded that cholesteryl ester presents a promising molecular marker for future prostate cancer diagnosis.

Schulze et al. [76] presented a study on chemical imaging of the cellular nucleus and its substructures. The Raman information was evaluated in comparison to differential interfering contrast images and images of nuclear stains. Based on pyrimidine and DNA O–P–O stretch vibrations (783 cm^{-1}) and RNA O–P–O stretch vibrations (809 cm^{-1}), chemical maps showed the distribution of all nucleic acids in the nucleus in general as well as subcellular RNA clusters. Furthermore, the protein distribution based on the phenylalanine band 1003 cm^{-1} was found to be similar to subnuclear nucleic acid distribution. The authors introduce morphometric analysis of the nucleolus by Raman imaging of its area and subsequent size determination. With regards to cancer cells which often show large nucleoli due to their rapid proliferation [77], this approach could be implemented to evaluate drug effects on nucleoli size, shape, and number in chemotherapeutics.

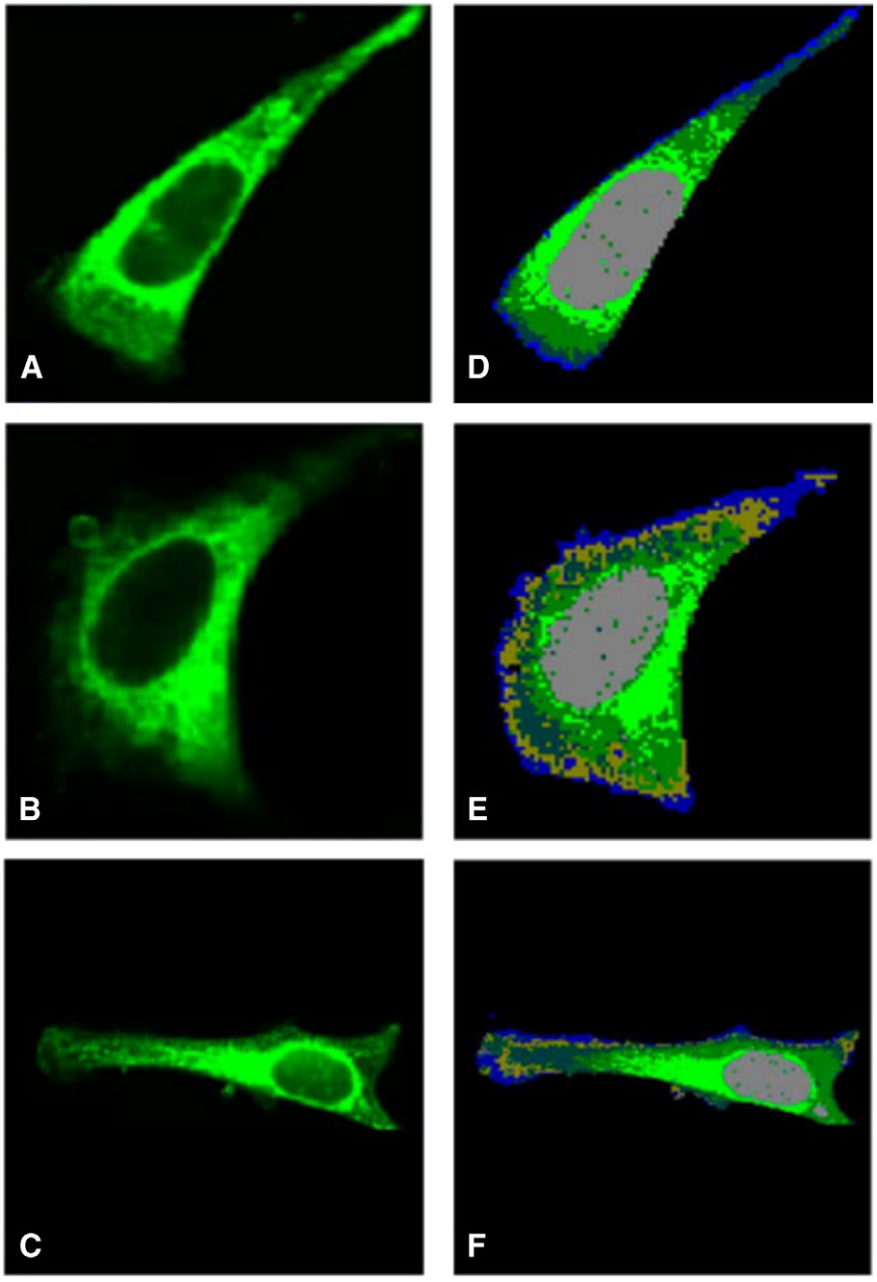

Fig. 4. Comparative study between fluorescence (A–C) and Raman imaging (D–F). Mitochondria rich areas are always depicted in green, proving the congruence of both analytical techniques. Reprinted from reference [49]. Copyright (2007), with permission from Elsevier.

Repeated imaging of living lymphocytes was reported by Pully et al. [78]. The same cell could be imaged 10–15 times in series before showing physical damage in the form of blebbing. Early and late acquired false color Raman images in the series only showed slight variation in DNA distribution due to internal motion of the nucleus. Bands of protein (2930 cm^{-1}) are also constant prior to cell blebbing. Raman difference spectra from all data cubes reveal a contribution of carotenoids with bands at 1524, 1154, and 1004 cm^{-1}. Carotenoids are mainly located in the cytoplasm as shown in a chemically selective image. Furthermore, carotenoids were detected in close approximation with lipid regions of the Golgi apparatus. A calibration curve of Raman scattering amplitude versus different concentrations of β-carotene allowed to estimate the molecular carotenoid concentration of 2.3 μM in a voxel of the image. The gradual decrease of carotenoids in the difference spectra as the image series proceeded was linked to the known photobleaching susceptibility of the molecules.

Human sperm cell composition is divided into head, neck and middle piece as well as the flagellum. Raman microspectroscopy was successfully applied for chemically selective imaging of the nucleus as a cell organelle, as well as the mitochondria rich middle piece and the neck. Subsequently, the damage of spermatozoa by ultraviolet radiation was tested. The middle piece was affected before damages of the nucleus became spectroscopically detectable [79]. Based on this study, Huang et al. [80] combined Raman microspectroscopy with image analysis for rapid identification of DNA integrity in sperm cells. To assess the quality of sperm cells for *in vitro* fertilization, vibrational marker modes of Raman spectra taken from sperm cells were identified by Huser et al. [81], as improperly packed DNA often accompanied by aberrant sperm head morphologies has been correlated to male infertility. The intensity

of the band at 785 cm^{-1} originating from cytosine breathing modes as well as from the DNA backbone marks the efficiency of the DNA packaging process. The lower the intensity, the higher the protein binding responsible for the packaging process. The protein amount was assessed by the intensity of the methylene deformation mode at 1442 cm^{-1}. As an internal independent marker for DNA–protein complex quantification the band at 1092 cm^{-1} (DNA backbone vibration) was chosen. Although the DNA–protein ratio could successfully be determined for normal and abnormally shaped sperm cells, the relative protein content per cell as well as DNA packaging efficiencies covered a rather wide range.

Wang et al. [82] acquired Raman spectra from different cells guided by confocal images to detect distinguishable spectral features of HaCaT cells, melanocytes and their malignant counterparts' squamous cell carcinoma and melanoma cells, respectively as a potential diagnostic tool in dermatology. The differences were presented by plotting difference spectra and discrimination analysis was supervised by generating so called receiver operating characteristic (ROC) curves.

Differences in morphological features of breast carcinoma cells (MCF-7/NeuT) and their doxycycline hyclate induced oncogenic senescent alteration were shown by Raman imaging displayed as varying CH-peak intensities as well as hierarchical cluster analysis images [83]. Structural modifications in the nuclear envelope showed to be specific for unsaturated lipid in the membrane. While control cells possess a combination of *trans* and *cis* unsaturated membrane lipids, their senescent counterparts contained a high contribution of unstable *cis* isomers in the nuclear membrane.

In this section, Raman mapping for single cell imaging was introduced. An overview of representative peak positions in the Raman spectrum of cells has been given. Thereby, the reader can follow the band assignments used in different studies to identify and consequently visualize subcellular structures in different cell types. A few studies based on cancer and differentiation of cancer cells and their malignant counterparts were also discussed. However, for further reading on Raman spectroscopy for diagnostic purposes and physiological investigations the reader is referred to themed articles in this issue.

4. Uptake of drug and nutrients in solution

In pharmaceutical therapy, drugs may also be administered in solution without any specific carrier, if bioavailability and drug stability are reasonable. Furthermore, upon carrier evaluation, comparative studies with the simple drug solution are often performed. However, sensitive and specific imaging of small dispersed molecules is highly challenging. Here, functional groups such as alkyne and deuterium have gained attention as potential markers to increase the Raman sensitivity of the molecules of interest as these groups display Raman peaks in the silent region of the cell spectrum (1800–2800 cm^{-1}).

Besides their spectroscopic feature, alkyne groups (C ≡ C) display chemical advantages. They are small and barely existent inside cells, thus considered to be exogenous [84]. Furthermore, alkynes are biorthogonal [84,85] meaning they are inert to reactions with endogenous biomolecules. The term alkyne-tag Raman imaging was introduced by the Sodeoka group [85]. Yamakoshi et al. [86] utilized 5-ethynyl-2′-deoxyuridine (EdU) a thymidine analog as an alkyne-tagged probe for chemically selective monitoring of cell proliferation. EdU was reported to be easily incorporated into cellular DNA during replication. Furthermore, it accumulates in the nucleus and is thus suitable to measure *de novo* DNA synthesis [87]. Due to the introduction of the alkyne group in the 2′-deoxyuridine molecule, a Raman peak in the silent region of the cell spectrum arises. To eliminate any extracellular molecules, HeLa cells incubated with 20 μM EdU for 6 h were washed prior to Raman microscopy analysis. False color Raman maps were reconstructed from bands at 749 cm^{-1} (cytochrome c) [21], 2849 cm^{-1} (lipids) and 2123 cm^{-1} (EdU). Contrary to treated cells, control cells did not reveal any alkyne peaks (Fig. 6A). The localization of EdU in the cell nucleus was confirmed

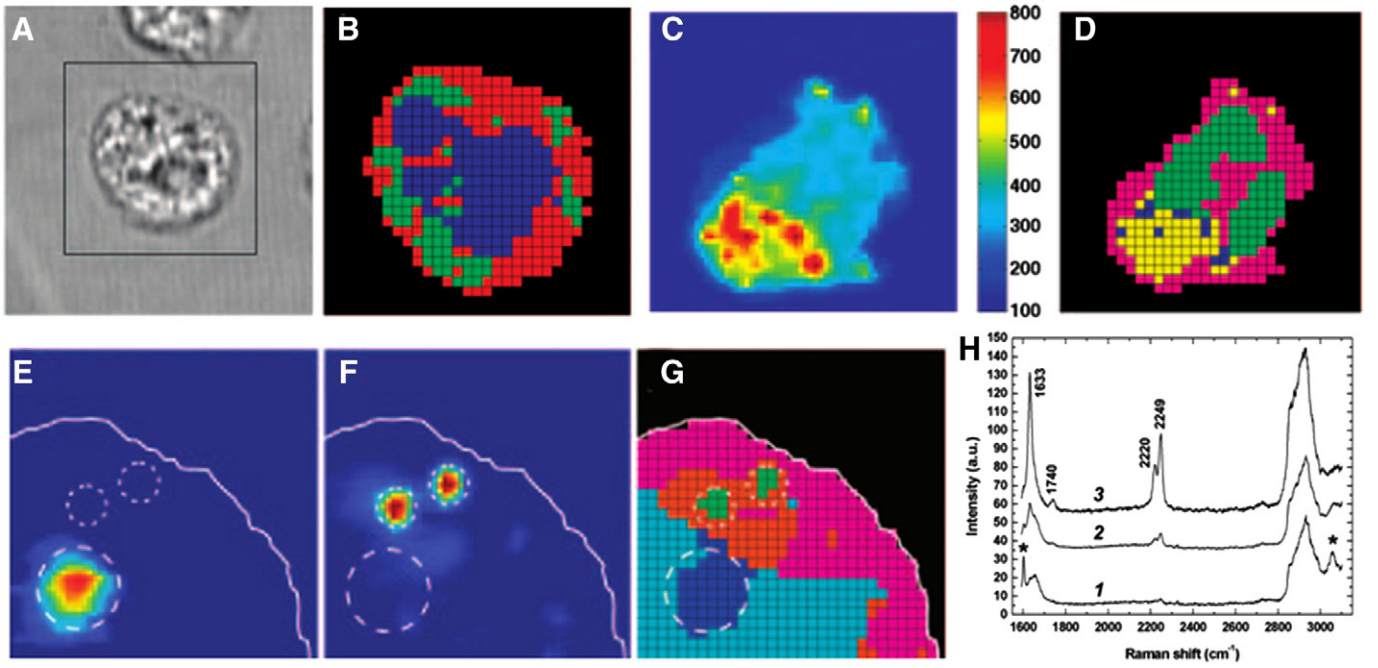

Fig. 5. Formation of lipid bodies in neutrophils. Neutrophils do not show lipid bodies until exposed to arachidonic acid (top row). Light microscopy images of a neutrophil (A) and corresponding cluster image (B). Colors are assigned to cytoplasm (green, red) and nucleus (blue). Lipid bodies form upon external arachidonic acid supply. Raman intensity map constructed for band at 1658 cm^{-1} (C) and corresponding cluster image (D). Lipids are displayed in blue, nucleus in green and cytoplasm in magenta. Lipid bodies reassemble around phagocytosed polystyrene beads (bottom row). Intensity maps for Raman bands at 1000 cm^{-1} (polystyrene, E) and 2200–2280 cm^{-1} (deuterated arachidonic acid (AA-d_8), F), as well as false color cluster map (G). Cluster colors blue, orange, and green are assigned to spectra 1, 2, and 3, respectively in H. Polystyrene peaks are highlighted with an asterisk. Adapted from reference [44]. Copyright (2005) National Academy of Sciences, USA.

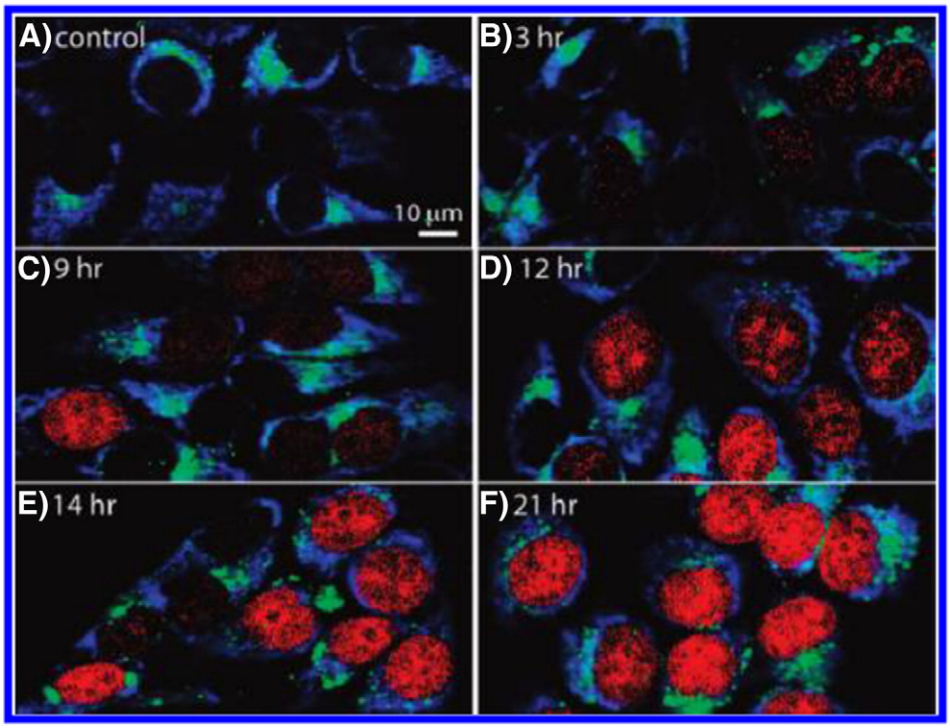

Fig. 6. Time-course false color Raman images of HeLa cells cultured in the presence of 5-ethynyl-2′-deoxyuridine (EdU). Control cells are cultured without EdU (A). Raman images at different time intervals show an increase of EdU containing cells (B–F). Colors are assigned to Raman bands of EdU (red, 2123 cm^{-1}), lipids (green, 2849 cm^{-1}), and cytochrome c (blue, 749 cm^{-1}). Reprinted with permission from reference [86]. Copyright (2011) American Chemical Society.

by fluorescence images after tagging EdU with a dye. Subsequently performed real-time Raman investigations of active DNA synthesis showed an increasing number of EdU positive cells (Fig. 6 B–F). According to the reported doubling time of 20 h for HeLa cells [88,89] almost all cells in the Raman image acquired after 21 h showed EdU in their nuclei.

Furthermore, various alkynes were investigated, showing that Raman intensity and Raman shift were highly dependent on the pattern of substituents [85]. Thus, it is possible to design two alkyne tagged molecules for simultaneous detection in the same cell sample. This was shown in a study of HeLa cells incubated with EdU (40 μM) and AltQ2 (2 μM), a coenzyme Q analog. The corresponding alkyne peaks located at 2122 cm^{-1} (EdU) and 2248 cm^{-1} (AltQ2) in the Raman spectrum could be easily discriminated.

Recently, a study of Yamakoshi et al. [90] was published introducing another mitochondrion-targeting Raman probe called MitoBADY. Bisarylbutadiyne (BADY) providing the alkynyl structure was linked to the known mitochondrial targeting moiety triphenylphosphonium. HeLa cells were incubated with MitoBADY (400 nM) and the substance was detectable (2220 cm^{-1}) inside the cells within 5 min. Simultaneous detection of cytochrome c (751 cm^{-1}) showed congruent cellular distribution.

A broad study of alkyne tagged biomolecule visualization in different cell types among others was performed by Wei et al. [84]. To overcome time consuming image acquisition, the authors used stimulated Raman scattering microscopy, as the concept of ATRI is applicable to non-linear Raman techniques as well. The metabolic uptake of EdU (100 μM) was imaged (2125 cm^{-1}) during *de novo* DNA synthesis, whereas RNA transcription and turnover was analyzed with 5-ethynynl uridine (2 mM), an analog of the ribonucleoside uridine. Newly synthesized proteoms within methionine starved HeLa cells were visualized by supplementing the cell culture medium with 2 mM of an alkyne-tagged analog of methionine called L-homopropargylglycine. The formation of numerous lipid droplets indicating a transformation into foam cells was shown after incubation of THP-1 macrophages with 17-octadecynoid acid (17-ODYA, 400 μM). Finally, the penetration of the antifungal drug terbinafine into mouse ear tissue was investigated. Due to the internal alkyne of the drug molecule it could be easily detected by following the Raman peak at 2230 cm^{-1}.

Erlotinib is a chemotherapeutic drug which selectively inhibits the epidermal growth factor (EGF) receptor. Its chemical structure comprises an alkyne group, which contributes a Raman signal at 2110 cm^{-1} to the compounds spectrum. Thus, the drug can easily be differentiated from cell spectra due to its internal marker. El-Mashtoly et al. [91] studied the uptake of erlotinib into colorectal adenocarcinoma cells (SW480). After 12 h of incubation with drug solution (100 μM), erlotinib was detected in the cell periphery by Raman imaging. To increase solubility and transport, the drug was dissolved in 6% captisol, a polyanionic β-cyclodextrine derivative in water. The selective peak at 1053 cm^{-1} of this enhancer was not detected in the Raman spectrum of internalized erlotinib. However, spectral changes between 1170–1595-cm^{-1} among reference and internalized drug were observed. These shifts were correlated to drug metabolism within cells, and desmethyl-erlotinib was spectrally identified as the metabolite in this case.

Due to similar chemical properties of isotopes like deuterium (^{2}H) or ^{13}C and their natural counterpart, isotopes are used to label and trace biomolecules like proteins, nucleic acids or lipids in cell biology. Van Manen et al. [92] incubated HeLa cells with deuterium labeled amino acids and investigated their uptake and incorporation into cellular proteins over time. Tyrosine and methionine were followed by their CD-stretch Raman bands (2000–2300 cm^{-1}), whereas phenylalanine was traced by using its characteristic band at 1001 cm^{-1}, which shifts to 959 cm^{-1} due to the introduction of deuterium. Isotope related Raman signals were detectable inside HeLa cells after 8 h of incubation and further increased with time. The spatial distribution of unlabeled and isotope-labeled proteins was found to be similar based on Raman imaging.

For studies of lipid metabolism inside cells, stable isotopic labeling of fatty acids is required for their differentiation from their native counterparts as done by Matthäus et al. [93]. They utilized macrophages (differentiated THP-1 monocytes) to study uptake dynamics and distribution of fatty acids and potential foam cell formation, which is considered as a first indicator for atherosclerosis. Serum albumin complexed deuterium labeled palmitic and oleic acid (400 μM each) as well as cholesterol (50 μM) were fed to macrophages. Fatty acids were continuously taken up by macrophages until after approximately 30 h the entire cytosol was filled with lipid droplets. Foam cell formation was observed in this late stage of incubation. The gradual increase of engulfed lipids was quantitatively evaluated by plotting the CD/CH ratio of spectra normalized to CH-scattering intensities against time. In contrast, sufficient signal intensity of deuterium labeled cholesterol was only detectable after 24 h of incubation. Due to an increasing signal intensity at 1745 cm^{-1} assigned to C=O-stretch vibrations of carbonyl groups over time, the authors postulated that fatty acids and cholesterol are possibly esterified and stored as triglycerides in lipid droplets. This assumption was supported by an enzymatic assay.

Overall, Raman studies of drug or nutrient solutions are sparse. This is mainly due to the fact that detection of finely dispersed molecules is challenging. Thus, rather high concentrations have to be applied to reach a sufficient accumulation inside the cell for detection. In the presented studies all molecules were equipped with an internal marker which mainly contributed Raman bands in the silent region of the spectrum making detection feasible.

5. Uptake of particles and carrier systems

Many nanocarriers have been developed intended for intracellular drug delivery. Besides the therapeutic purpose of these small systems, potential cytotoxicity aspects have to be considered. The word nanotoxicity has become standard terminology in discussions of cellular interaction with nanosized particles, partly due to the immense use of non-biodegradable engineered particles in material sciences. One important question is the potential internalization of such particles and their intracellular fate. Here, drug carrier systems have to be considered as well as other nanoparticles such as carbon nanotubes and inorganic particles.

Liposomes are small vesicles with a phospholipid bilayer membrane surrounding an aqueous core. As phospholipids are a natural component of cells, the sensitivity for biochemical imaging of liposomes in cells has been increased by using deuterated phospholipids for liposome preparation [94,95]. The covalently bound deuterium is not perturbing with the analysis of live cells. Due to the introduction of CD-bonds, Raman bands of the CD-stretch vibrations in the silent region between 2000–2300 cm^{-1} become a prominent structure while Raman band intensities of CH-bonds decrease making liposome detection feasible.

The uptake of liposomes made of deuterated 1,2-distearoyl-*sn*-glycero-3-phosphocholine (DSCP) in human breast adenocarcinoma MCF-7 cells was studied in direct comparison to surface modified DSCP-liposomes [94]. After 6 h of incubation only few cells showed liposome inclusion, whereas liposomes were internalized in all investigated cells after 12 h indicating that cellular uptake reaches a plateau. Liposome internalization was chemically selective displayed in lateral overview images of CH- and CD-stretching intensities, where CH-vibrations represent the most prominent band of the protein spectrum in the cytoplasm and CD-bands represent the liposomes. To exclude liposome absorbance on the cell surface, depth images of the xz-direction were presented additionally. The modification of the liposomal surface with the cell penetrating peptide TATp yielded an accelerated uptake. Thus, TATp-liposomes were localized in the cell periphery around the membrane after 3 h and a deeper penetration into the cell body of all investigated cells after additional 3 h.

Chernenko et al. [95] prepared three different types of cationic liposomes with a size of ~175 nm. HeLa cells were incubated for 1, 3 and 6 h with suspended liposomes prior to Raman imaging. 1,2-dioleoyl-3-trimethylammonium-propane (DOTAP) and stearyl amine (SA) modified cationic liposomes did not show an increased penetration nor a variable cell translocation pattern over time. Rather than being compartmentalized, liposomes stayed in the periphery of the cell forming aggregates. Liposomes modified with stearyltriphenylphosphonium (STPP) known for mitochondria affinity, led to different intracellular behavior of liposomes and an enhanced uptake. The visual observation of STPP-modified liposomes enriched in mitochondria-rich perinuclear regions was also observable in the endmember spectra of the VCA. Here, the spectrum derived from the mitochondria-rich area showed distinct CD-stretching vibrations from the liposomes.

Poly(lactic-*co*-glycolic acid) (PLGA) is an often used biodegradable polymer for nanoparticle preparation. Its degradation is mainly driven through hydrolysis of the ester linkages or/and enzymatic degradation [96,97]. The ester bonds are represented by the carbonyl stretching vibrations at 1768 cm^{-1} in the Raman spectrum of PLGA [98]. The depletion of this bond was utilized to monitor phagocytozed PLGA microsphere degradation. Difference spectra calculated from spectroscopic data after Raman imaging showed a 30% decrease in the ester bond intensity two weeks subsequent to incubation start. When PLGA microspheres were cultivated in absence of macrophages, no signs of degradation were observable.

Mapping of intracellular PLGA nanoparticles and their degradation was also performed by Chernenko et al. [99]. Due to the smaller particle sizes, degradation was observed after 3 to 6 h after renewing the cell culture medium and hence terminating further particle incorporation. Here, the intensity decrease of the ester peak at 1765 cm^{-1} was again taken as a marker for PLGA hydrolysis until fully vanished from the spectral data set. The decrease of the ester peak goes along with an increase of a lipid characteristic peak at 1740 cm^{-1}, suggesting that PLGA nanoparticles are enclosed in vesicles. A similar study was conducted on the uptake and degradation of PCL (poly(ε-caprolactone)) nanoparticles [99]. PCL is another biocompatible and biodegradable polymer with slower degradation kinetics than PLGA [100,101]. After an incubation time of 7 h, all HeLa cells showed PCL particle inclusion. Longer incubation times did not lead to an increased intracellular concentration. However, a formation of intracellular lipid droplets as a consequence of nanoparticle internalization was detected. Spectral end members of the VCA analysis of the Raman spectral data cube revealed phospholipid-characteristic peaks as well as the band at 1745 cm^{-1} corresponding to the ester bond. Thus, the authors concluded that the development of inclusion areas is linked to the formation of endocytotic vesicles upon particle engulfment. Spectral signatures became less pronounced over 17 h postincubation, indicating PCL degradation, but did not vanish entirely over the investigated time period.

Romero et al. [102] also discovered the co-localization of lipid bodies and internalized PLGA nanoparticles. They proved the suitability of Raman spectroscopy for simultaneous detection of nanoparticles and lipid cell bodies by identifying reference peaks of pure PLGA nanoparticles and lipid bodies in spectra taken from hepatocarcinoma cells (HepG2) incubated with PLGA nanoparticles. The particle uptake was subsequently investigated by spectral acquisition along the z-axis of cells previously exposed to nanoparticles. Stabilization of PLGA particles with BSA led to higher cellular engulfment than stabilization with poly(ethylene imine) (PEI).

The same group studied the intracellular delivery of doxorubicin from PLGA nanoparticles [103]. Here, Raman spectra taken from the nucleus of treated HepG2 cells revealed a drastic change of DNA/protein ratio calculated from the nucleotide band at 1338 cm^{-1} and the amide III band (1200–1290 cm^{-1}). This effect was only observed when cells were incubated with doxorubicin loaded particles and not for the empty carrier, as doxorubicin intercalates in DNA strands inhibiting the cell replication process.

PLGA nanoparticles with a layer-by-layer coating of the antibody antiTNF-α were investigated for intracellular delivery of the antibody

[104]. First, Raman spectra of cell cytoplasm, antibody and uncoated nanoparticles were compared to Raman spectra taken from HepG2 cells incubated with antiTNF-α PLGA nanoparticles to identify their chemical signatures. Outstanding Raman bands between 1500 and 1700 cm^{-1} originating from proteins and C = O -stretch vibrations of the antibody were identified. A line scan across the cell was carried out to analyze component distribution. Cells exposed to antiTNF-α PLGA nanoparticles revealed a major association of antibody with lipid signal from the cell and only a small fraction coincided with nanoparticle signal. Thus, the authors concluded that antiTNF-α is delivered into the cell, released from its carrier and preferentially localized in lipid rich regions of the cytoplasm.

Another loaded PLGA system for intracellular delivery was studied by Matthäus et al. [105]. Despite a low loading efficiency of β-carotene (0.063 μg β-carotene per mg PLGA), the Raman spectra of the β-carotene loaded PLGA nanoparticles were dominated by bands characteristic for β-carotene (1510, 1153 and 1004 cm^{-1}) due to the resonance Raman effect of the molecule making intracellular detectability feasible (Fig. 7). Mouse fibroblasts (NIH-3 T3) showed a maximal uptake after 3 h of incubation with β-carotene PLGA nanoparticles. Analysis of the spectral data set by VCA revealed an encapsulation of particles in endosome like vesicles after cellular engulfment due to the superposition of spectral feature characteristic for β-carotene as well as lipid structures (Fig. 7 C). An increased fluorescent background of spectra associated with particle distribution suggested the beginning β-carotene degradation within the investigated time period of 9 h.

Recently, in a study of Verderio et al. [106] PLGA nanoparticles were used as a carrier for intracellular delivery of the antiproliferative compound ASC-J9 (1,7-bis(3,4-dimethoxyphenyl)-5-hydroxyhepta-1,4,6-trien-3-one). The loaded particles were taken up by human breast cancer cells (MCF-7) within 24 h as shown by confocal Raman microscopy experiments. Pseudo-colored Raman maps depicted intracellular particle localization with respect to nucleus and vesicles based on characteristic Raman bands for cytoplasm (1450 cm^{-1}, CH deformation in proteins and lipids), DNA (788 cm^{-1}, O–P–O backbone stretch), and fatty acids (1300 cm^{-1}, CH_2 vibration). Classical least square analysis utilizing a nanoparticle reference spectrum showed a co-localization with intracellular vesicles in some areas indicating an endosomal pathway active in particle uptake.

As cell penetrating peptides (CPP) are quickly internalized by cells, these small molecules have shifted into the focus of pharmaceutical research due to their potential for intracellular delivery. Thus, cell penetrating peptides can be conjugated with, encapsulated by or physically adsorbed to carrier systems like polymeric nanoparticles, CNTs, dendrimers, micelles, solid lipid nanoparticles or liposomes, imaging agents including gold nanoparticles and quantum dots as well as other cargo like nucleic acids, proteins and drug molecules. However, prior to studying the use of CPPs as a vector to channel their cargo inside cells, more information about the intracellular localization of CPPs as well as their microenvironment and secondary structure postmembrane penetration has to be gained. In this context, Ye et al. [107] investigated penetratin a 16-residue CPP, its distribution and secondary structure within human metastatic melanoma cells (Sk-Mel-2) by Raman microscopy. In cellular Raman spectra, a pronounced vibrational band at 1003 cm^{-1} is generally observable. It is associated to the aromatic ring breathing modes of the amino acid phenylalanine [108]. Furthermore, the enormous peak contribution of other endogenous proteins hinders the intracellular detection of exogenous peptides. Thus, Ye et al. [107] used ^{13}C atoms to label the phenylalanine residue of penetratin. As a consequence, the vibrational band of the ring-breathing mode shifted from 1003 cm^{-1} to 967 cm^{-1} as reported in literature [109] and tracing of the rapid entry of the CPP into cell cytoplasm as well as into the nucleus became feasible. After calculating difference spectra and principal component analysis, the peptide Raman spectrum was resolved from the cellular background signals. Thus, based on the amide I band position in the resolved spectra, the secondary structure of penetratin was determined to be mainly random coil and β-strand. As CPP spectra could not be concomitantly detected with lipid Raman signatures paired with the quick intracellular detection within 2–3 min after exposure, a non-endocytotic internalization route was proposed.

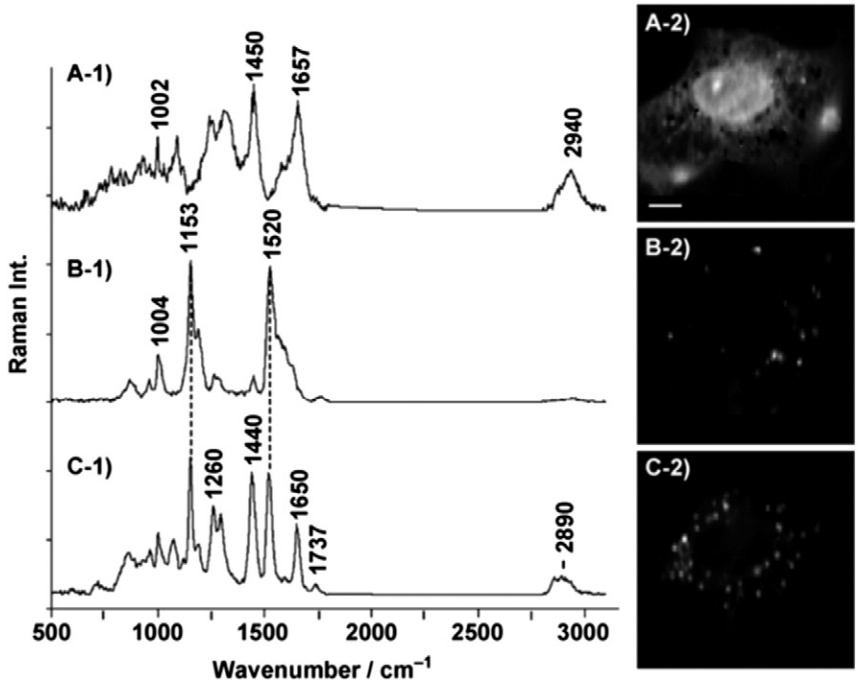

Fig. 7. Cellular uptake of β-carotene loaded PLGA nanoparticles. Raman spectra and corresponding maps are aside showing protein features (A), β-carotene PLGA nanoparticles (B), and β-carotene and lipids in superposition (C). Scale bar is 10 μm. Reprinted from reference [105].

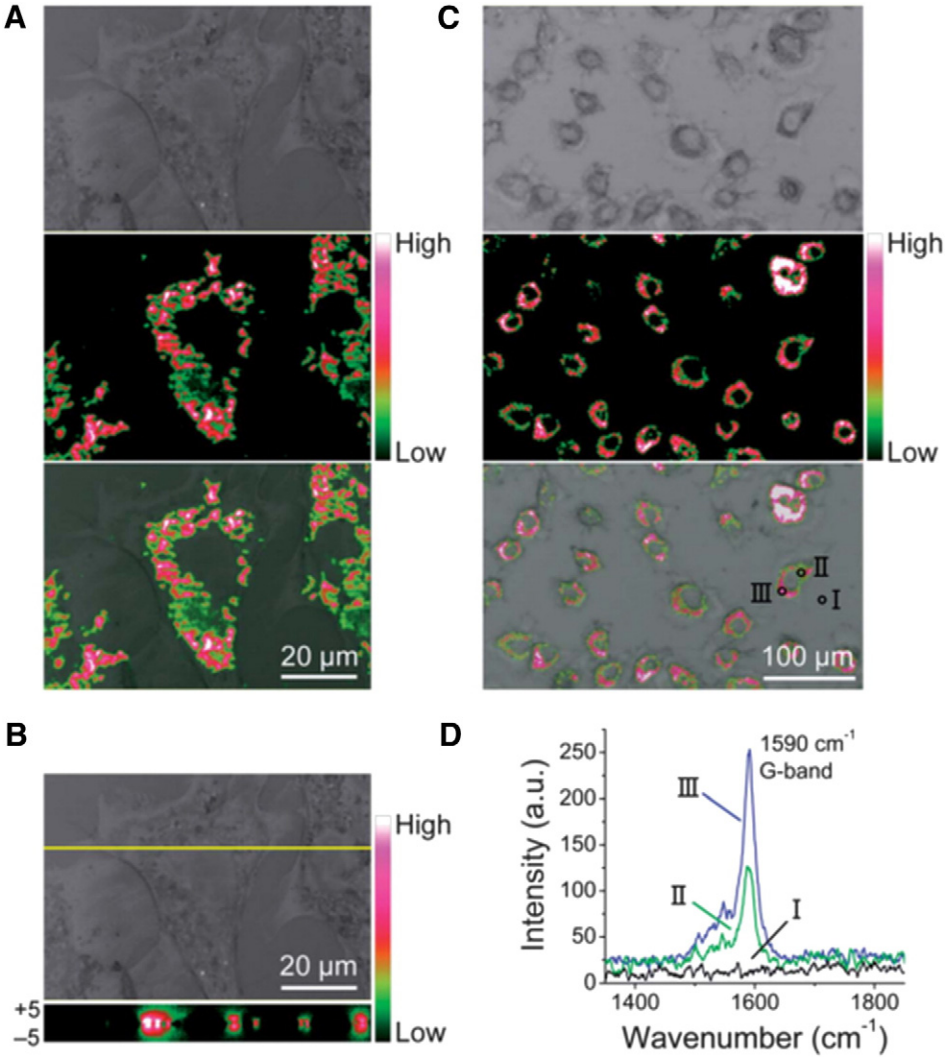

Fig. 8. Stem cell labeling with collagen coated single-walled carbon nanotubes for Raman microscopy. Images A and C show phase contrast, Raman and merged images, whereas xz cross section investigations (B) only depict phase contrast and Raman image. Images are generated by the intensity of the G-band of carbon (D). Red refers to high and green to lower band intensities, and thus accumulation densities of nanotubes within the cells. Adapted from reference [113] with permission of The Royal Society of Chemistry.

The supervision of stem-cell based therapy relies on the discrimination between implanted and host cells. State of the art for stem cell labeling and tracking is the utilization of genetically encoded luciferase and fluorescent proteins [110–112] necessitating complex genetic modifications of the stem cells. Mao et al. [113] introduced collagen coated single-walled carbon nanotubes (Col-SWCNTs) for long-term stem cell labeling. The authors used confocal Raman imaging to visualize the internalization of Col-SWCNTs by human bone marrow-derived mesenchymal stem cells (hMSCs) (Fig. 8). The focal plane for spectral acquisition was set to the plane containing the cellular nucleus. The G-band at 1590 cm^{-1} was used for SWCNT detection. Lateral and depth profile false color Raman images revealed internal SWCNT localization around the nucleus in higher and lower density regions in the cell cytoplasm (Fig. 8 A, B). The same distribution patterns were observed when multiple cells were mapped (Fig. 8 C). Despite the high number of internalized Col-SWCNTs, neither obvious cytotoxic effects nor influences on the differentiation potential of hMSCs were observed. Continuous mapping of the labeled hMSC culture over 14 days showed a decrease of SWCNT per cell over time detected by a drop in signal intensity of the CNT G-band, which is a direct effect of dilution by prolonged cell division. Nevertheless, Raman signal intensity obtained from labeled hMSC cells was still high enough, thus indicating the potential of Col-SWCNT as suitable labels for stem-cells therapy monitoring.

Further uptake studies of SWCNTs into hMSC cell were performed by Holt et al. [114]. They stabilized their SWCNT with bovine serum albumin (BSA) and included a second cell line namely HeLa cells into their study. A high dispersive degree of SWCNTs through BSA stabilization was confirmed by NIR fluorescence measurement, as bundling on CNTs is known to cause quenching of the inherent fluorescence [115]. Raman maps showed the uptake of BSA-dispersed SWCNTs into the cytoplasm of both cell types, where the majority was located in the perinuclear region. However, the positioning of some SWCNTs toward the cell boundary, indicate an interaction of SWCNT and filamentous actin [116]. Superimposed phase contrast images on Raman maps did not reveal any harmful cellular effects despite very high local SWCNT concentrations up to 15 μg/mL. Although the global concentration of SWCNT per cell is high, only ≈0.1% of the cellular volume was hold by SWCNTs. Raman imaging in different z-positions visualized the SWCNT distribution throughout the cell body. A rather strong intensity just above the cell was also rated as an indication of possible interactions with the cell membrane.

Besides the uptake of PLGA nanoparticles the Moya group [102–104] also investigated the uptake of oxidated carbon nanotubes (CNTs) [117]. Due to spectral acquisition along the z-axis through a cell previously exposed to CNTs, Raman bands from cell cytoplasm, organelles and CNTs can be recorded simultaneously. The D and G-band at 1350 and

1585 cm^{-1}, respectively, were chosen for CNT tracking. Independent of z-position, CNT associated bands were only found concomitantly with CH_3-stretching modes, which are typical for proteins and generally represent the cytoplasm. Thus, in contrast to analytical results from PLGA nanoparticle internalization studies, CNTs were not associated with lipid bodies.

In medical inorganic chemistry, research attention has been drawn towards metal complexes with therapeutic activity. However, it was shown that fluorescence labeling alters the biodistribution and properties of ruthenium–bipyridyl complexes [118]. Thus, fluorescence microscopy is inapplicable for cellular internalization studies, as the native behavior of the metal complex is changed. Consequently, attaching fluorescent markers to other metal complexes of interest might cause analog hindrances. Meister et al. [119] studied the uptake of the manganese-based CO-releasing molecule $[Mn(tpm)(CO)_3]Cl$ (tpm = tris(1-pyrazolyl)methane) into HT-29 colorectal adenocarcinoma cells. This metal–carbonyl complex shows a strong Raman band in the silent region of the cell spectrum due to the C ≡ O stretching vibrations. Therefore, it is well suited for confocal Raman microscopy analysis and fluorescence microscopy can be neglected. In aqueous environment when the complex is dispersed in cell culture medium for incubation, the peak shifts from 1944 cm^{-1} to 1963 cm^{-1} but stays within the silent region not hampering analysis. Reconstructed false color Raman images from CH-stretching vibrations and C ≡ O-stretching vibrations between 2800–3050 cm^{-1} and 1945–1965 cm^{-1}, respectively, visualize the association of the metal–carbonyl complex primarily with the nucleus and the nuclear membrane. An absorbance on the cellular surface was excluded by cross-section Raman images. In addition to cellular internalization, a photoinducable cytotoxic activity of $[Mn(tpm)(CO)_3]Cl$ against cancer cells has been reported in literature [120] making the complex a promising candidate for cancer therapy.

Adenocarcinoma cells (SK-BR-3) were incubated with pegylated gold nanorods overnight and subsequent Raman mapping visualized the successful internalization [121]. Cluster analysis differentiated between cell nucleus, cytoplasm, cell membrane and gold nanorods. The respective cluster spectrum for gold nanorods revealed the typical fluorescence signal in the fingerprint region. Thus, the Raman signals from the cell were masked in the fingerprint region in areas were gold nanorods were localized. However, cellular spectral information could be extracted from the superimposed fluorescence by multivariate methods. By calculating the spectral differences between this disentangled spectrum and cellular spectra from SK-BR-3 control cells, a shift in the lipid–protein ratio was observed. As the lipid peak at 2856 cm^{-1} increased while the protein bands (2950–2965 cm^{-1}) dropped in intensity, the authors concluded that lipid vesicles encapsulating PEG-gold nanorods were possibly formed.

Besides drug-loaded carriers in nanometer size, numerous nanomaterials confront the human body as non-active compounds of therapeutics like tablets or within food and consumer products. For instance, the wide use of titanium dioxide nanoparticles in daily consumer products as well as their use as food additive raises the question about their fate upon contact with the human body. Kann et al. [122] visualized particle uptake into human oral buccal mucosa cells (TR146) in lateral (xy) and cross section (xz/yz) images (Fig. 9). As some particles were even detected in close approximation to the cell nucleus, genotoxic consequences of the TiO_2 invasion have to be considered in future experiments. Besides uptake via the oral route, pulmonary exposure is another entrance way for nanoparticles into the human body. Thus, Ahlinder et al. [123] chose lung epithelial cells (A549) to study the cellular uptake of titania and goethite (α-FeO(OH)) nanoparticles. Raman analysis revealed that 37%, 32% and 23% of voxels contained a spectral contribution from the respective particles at 638 cm^{-1} for TiO_2, 388 cm^{-1} for α-FeO(OH) or a band mixture and cell nucleus corresponding signatures. Similar findings of nanoparticle association with cell nuclei in both studies highlighted the importance of further studies on interactions of these nanoparticles with DNA on the molecular level to gain insight on potential genotoxic effects.

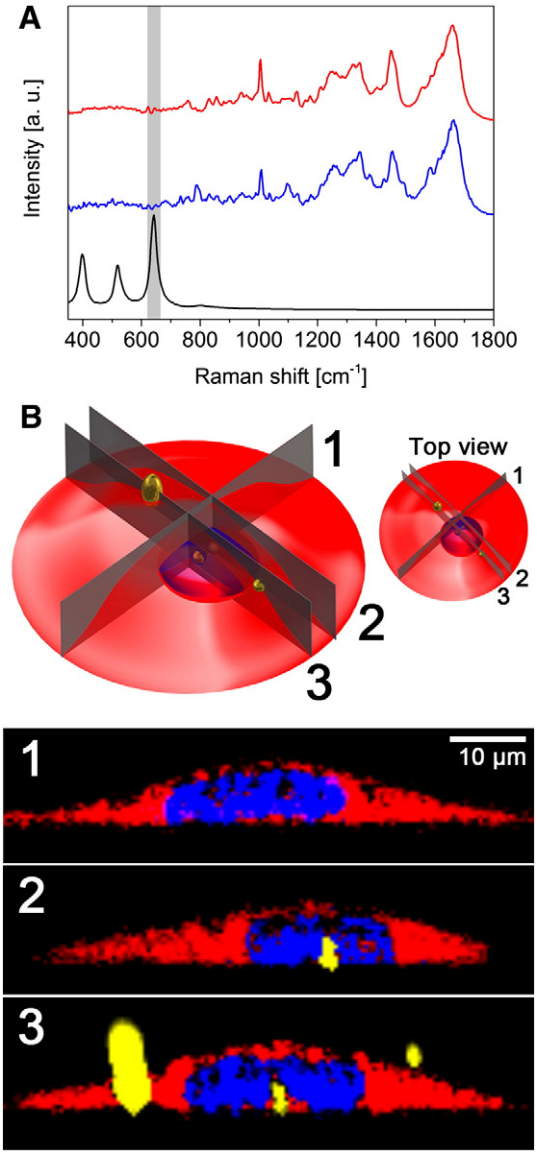

Fig. 9. Titanium dioxide (TiO_2) engulfment into oral buccal cells. A) Spectra of cell cytoplasm (red), nucleus (blue) and TiO_2 (black). The peak for TiO_2 discrimination is highlighted. B) Sketch of a cell showing the vertical planes for Raman investigations. Cross section Raman images showing multiple particle engulfment states. Colors are assigned according to spectra (TiO_2 is depicted in yellow). Adapted from reference [122] — Reproduced by permission of The Royal Society of Chemistry.

In this chapter, Raman imaging studies on cellular interactions with nanosized particles ranging from drug delivery systems up to commercialized nanomaterials have been summarized. As Raman imaging relies on the detection of molecular vibrations, the material of the nanosized particles has to contribute other bands than cells to be distinguishable and thus making analysis feasible.

5.1. Surface enhanced Raman scattering microscopy for cellular applications

So far, only studies based on spontaneous Raman microscopy for cellular investigations have been discussed. Due to emerging scientific interest in Raman microscopy a variety of linear and non-linear techniques based on the Raman effect have been introduced for cellular

applications. The non-linear Raman techniques such as coherent anti-Stokes Raman scattering microscopy are discussed in detail elsewhere in this issue.

The low Raman scattering efficiency of an analyte especially of biological nature can significantly be increased by locating it near the surface of a noble metal nanostructure. This process is known as surface-enhanced Raman scattering (SERS) and the amplification of the received signal overcomes the limitation of the inherently low Raman scattering efficiency of Raman spectroscopy [124,125]. Laser irradiation of metallic nanostructured surfaces give rise to an additional electric field, which can become very large due to coupling to a surface plasmon. The plasmon frequency of the oscillating electrons results from a spatial confinement of electrons in metallic nanostructures. At this characteristic frequency a resonance response of the local electromagnetic field occurs. The intense localized surface plasmon fields responsible for scattering enhancement can be triggered in submicron metallic nanostructures such a gold and silver and interact with molecules in close vicinity [126]. Among other materials, especially gold nanoparticles have been used for SERS investigations of living cells [127–129]. Most common are spherical shaped nanoparticles, but other geometries such as nanorods [130], nanoflowers [131–134] or nanostars [135–137] have also been reported as SERS probes.

In general, there are two approaches to apply SERS probes for cellular investigations. They can either be directly linked to the sample molecule comparable to a fluorophor in fluorescence microscopy or they are applied in addition to the analyte to sense it. As Raman scattering is enhanced by orders of magnitude in SERS compared to spontaneous Raman spectroscopy, analytes can be detected in nM concentrations or even as single molecules [138], whereas spontaneous Raman spectroscopy typically requires concentration exceeding 1 mM [139]. If no analyte is directly probed, the metallic nanoparticles are generally decorated with Raman reporters such as 4-mercaptopyridine [134], 4-mercaptobenzoic acid [130,140], 4-aminothiophenol, or 4-thiochresol [126], thereby increasing the Raman reporters signal drastically making SERS imaging of cells feasible. Gregas et al. [126] compared the effect of silver nanoparticles labeled with different reporter molecules on cellular uptake efficiency. They observed that the choice of reporter molecule influences particle size, charge and chemical structure which are in turn important parameters determining cellular uptake. To improve stability as well as biocompatibility of metal nanoparticles encoded with Raman reporter molecules, the particles can be protected with a polymer coating made of silica or PEG, for example [141,142].

Graphene oxide metal nanoparticle composites have also been used for diverse SERS applications in cellular imaging. Graphene oxide is an excellent candidate for biomedical imaging due to its inherent fluorescence [143–145] and Raman scattering activity [140,146]. Gold nanoparticles were wrapped in a graphene oxide layer for SERS probing inside HeLa cells [147]. The particles were visualized with a higher contrast in cells due to the enhanced scattering of graphene oxide neighboring metal nanostructure than cells treated with just pure graphene oxide. These wrapped particles were also shown for efficient delivery of the drug doxorubicin into the cell.

One major application of SERS mapping for cellular applications is the detection of target structures through labeled SERS probes. Thus, additionally to reporter molecules, the nanoparticles can be coated with diverse antibodies to target and consequently visualize specific cell types [134,148,149]. A study by Liu et al. [140] showed the feasibility of SERS imaging to differentiate between folate receptor expressing cervix carcinoma cell line HeLa and the folate receptor negative lung cancer cell line A549. Images of HeLa cells exposed to folic acid decorated graphene oxide silver nanoparticles presented intense Raman signals on the plasma membrane as well as intracellular signals after a prolonged incubation time indicating an uptake of the nanoparticles. For A549 cells, which do not express the folate receptor, no particle association with the cells was observed. Gold nanorods conjugated with the Raman reporter 4-mercaptobenzoic acid and anti-epidermal growth factor receptor (EGFR) antibody were designed to localize the EGFR on the breast cancer cell line A431 [130]. EGFR is a widely used biomarker for therapeutic targeting of human cancers and thus, studying its expression on cell surfaces and its internalization pattern is of great value for developing therapeutic strategies. Due to the antibody-antigen interaction, EGFR distribution and cellular uptake could be non-invasively probed by SERS. In a similarly designed study, phenotypes of cancer cells were tested by SERS imaging after incubation of three different breast cancer cell lines (MDA-MB-468, KPL4, and SK-BR-3) with respective antibody conjugated silica-encapsulated hollow gold nanospheres [149]. As three different SERS-active nano tags malachite green isothiocyanate, rhodamine B isothiocyanate, and bis(2,3′-bipyridine)-(5-isothiocyanato-phenanthroline) ruthenium bis(hexafluorophosphate) were used as Raman reporters, rapid identification of cell phenotype was possible due to the different Raman shift of the tag molecules. Branched DNA-gold nanoaggregates have been utilized to discriminate between two biomarkers simultaneously expressed on the same cell surface by aptamer recognition instead of traditionally used antibodies [150]. To increase the intracellular delivery of nanoparticles cell penetrating peptides especially the so called TAT-peptide have gained attention in pharmaceutical sciences [151]. It was also used to enhance intracellular SERS imaging as the internalized amount of gold nanostars increased significantly when decorated with the cell penetrating peptide [137].

As SERS provides detailed spectral information from the local environment of the metallic nanostructures, it can be beneficial for the analysis of subcellular processes as well as for direct detection of analytes such as drug molecules.

Erythrocytes mainly contain hemoglobin which can be subdivided into two populations, namely cytosolic and submembrane hemoglobin [152,153]. Although hemoglobin exhibits strong Raman scattering, Raman spectra of erythrocytes generally correspond to cytosolic hemoglobin as the contribution of submembrane hemoglobin is negligible. To study exactly this submembrane hemoglobin Brazhe et al. [139] performed a SERS study enhancing the Raman scattering of hemoglobin by adding silver nanoparticles of different sizes to the cell suspension. Acquired Raman spectra showed increasing signal intensity with a decreasing particle size. The authors linked this phenomenon to morphological aspects of the cell membrane. Deeper parts of the membrane invaginations can be easier approached by tiny particles, thus SERS substrates locate closer to submembrane hemoglobin leading to higher SERS signal.

The central cell organelle is the nucleus. It holds among others the genetic information of an organism. Thus, it is a desirable target for drug delivery. Xie et al. [154] reported on effective localization of functionalized gold nanoparticles at the cell nucleus of HeLa cells. Subsequently, structural information of nucleic acids and proteins from the nucleus could be gathered from the acquired SERS data. Furthermore, the cells were incubated with the DNA intercalator 4′,6-diamidino-2-phenylindole (DAPI) and molecular vibrations from this subsequently introduced molecule were detected along with nuclear components, highlighting the potential of benefitting from this approach in drug delivery research.

Bálint et al. [155] monitored drug diffusion through the cell membrane of U87-MG cancer cells. Prior to adding the anti-cancer drug emodin (2 μM) to the cell medium, cells were incubated with SERS probes for passive implantation. They consisted of micrometer sized silica beads which were partly coated with colloid nanosized silver particles. Due to the micrometer size of the probe, a direct contact with the cell membrane was assumed. Raman bands at 1170 and 1132 cm^{-1} were identified as marker bands of emodin to monitor emodin diffusion through the cell membrane. The resulting diffusion curve was in agreement with standard fluorescence measurements.

Although the suitability of surface enhanced Raman spectroscopy has been demonstrated in numerous studies, the technique is also attributed with some pitfalls. Especially in live cell studies introduced

SERS substrates such as nanoparticles may modify cell properties. Furthermore, nanoparticle properties including size, shape and the position of the plasmon resonance affect the Raman enhancement [139]. Fujita et al. [156] studied the intracellular dynamics of gold nanoparticles in macrophages. The intracellular movement was successfully captured with spatial resolution in temporally resolved images, but also revealed a high fluctuation in Raman signal intensity. Thus, the position of a generated plasmon in relation to the scanning laser influences analytical results. Diffusion of the plasmon generating nanoparticles in the cell can also cause confusing information during analysis. Furthermore, the size of the plasmon is limited and consequently, the surrounding area which can be analyzed is restricted, too.

Overall, SERS shows a great potential especially for the investigation of cells, their subcellular structures and interactions with nanocarriers. The field of application broadens rapidly, however, the technique still has to mature. To gain a more detailed insight into this technique, we refer to the specialist article in this issue as SERS studies are too numerous for all-encompassing acknowledgment in this contribution. Nevertheless, the field cannot be neglected for cellular investigations.

6. Conclusion and perspective

Raman microscopy has successfully been applied to a broad range of investigations on the single cell level. Diverse subcellular organelles such as mitochondria, lipid bodies, nuclei, and nucleoli have been detected solely based on their inherent molecular vibrations. In addition, different stages in a cell live cycle from early stem cells to apoptotic changes were identified by confocal Raman microscopy without labeling. However, for accurate detection and monitoring of delicate processes like DNA synthesis and lipid metabolism, small molecular changes like the addition of alkyne groups or the exchange of hydrogen against deuterium atoms in the target molecule have to be performed. A major focus of current research studies is on the analysis of cellular interactions with particulate systems in terms of risk assessment as well as for the development and evaluation of novel carrier systems for therapeutic drug administration. The interaction of polymeric nanoparticles especially made of PLGA with various cell types was extensively studied including their degradation. Other inorganic nanoparticles as well as carbon based structures were also of great interest under the aspect of engineered nanomaterials and cytotoxicity or as contrast agents for long term imaging purposes. If such carrier systems are composed of molecules which also constitute cellular components, deuterated molecules have to be used for detection by Raman spectroscopy. Prominent examples are liposomes. They consist of phospholipids, which at the same time represent the main compound of the cellular membrane. Overall, confocal Raman microscopy is not restricted to specific cell types or carrier structures and its broad feasibility as an analytical technique was demonstrated in numerous studies. However, literature research also revealed that the technique is not a standard application in this research field and has by far not reached the current status of fluorescence microscopy. This is partially due to the fact, that confocal Raman microscopy analysis demands a precise knowledge, not only about the sample, but also about the operation of the microscope to record the spectral data set and even more important, the processing of the acquired spectral data set. Thus, scientists from multiple disciplines have to merge their expertise to perform successful research and benefit from each other. Another limitation for Raman imaging is the detection limit for substances. Studies on the single molecule level are impeded, thus cellular *in vitro* studies are often designed for higher doses of drugs and carriers than *in vivo* experiments would allow. Here, the Raman instruments have to be further optimized to enable a more sensitive detection.

In summary, confocal Raman microscopy has proven itself as a powerful analytical technique with high accuracy for the analysis of single cells and micro- to nanometer sized structures. It has found a variety of applications for diversified investigations of interactions of cells with drugs and carrier systems in the pharmaceutical field. With continuous improvement in technology and the growing acceptance of Raman microscopy, a further increasing number of studies can be expected in the future. These studies evidence a bright future of confocal Raman microscopy for spatially resolved chemically selective analysis in pharmaceutical and biomedical research.

References

[1] A. Aderem, D.M. Underhill, Mechanisms of phagocytosis in macrophages, Annu. Rev. Immunol. 17 (1999) 593–623.
[2] H. Hillaireau, P. Couvreur, Nanocarriers' entry into the cell: relevance to drug delivery, Cell. Mol. Life Sci. 66 (2009) 2873–2896.
[3] P. Lasch, A. Pacifico, M. Diem, Spatially resolved IR microspectroscopy of single cells, Biopolymers 67 (2002) 335–338.
[4] S. Verrier, I. Notingher, J.M. Polak, L.L. Hench, In situ monitoring of cell death using Raman microspectroscopy, Biopolymers 74 (2004) 157–162.
[5] E.D. Korn, R.A. Weisman, Phagocytosis of latex beads by Acanthamoeba. II. Electron microscopic study of the initial events, J. Cell Biol. 34 (1967) 219–227.
[6] H. Yamakoshi, A.F. Palonpon, K. Dodo, J. Ando, S. Kawata, K. Fujita, M. Sodeoka, Simultaneous imaging of protonated and deprotonated carbonylcyanide p-trifluoromethoxyphenylhydrazone in live cells by Raman microscopy, Chem. Commun. 50 (2014) 1341–1343.
[7] S. Mayor, R.E. Pagano, Pathways of clathrin-independent endocytosis, Nat. Rev. Mol. Cell Biol. 8 (2007) 603–612.
[8] D.M. Copolovici, K. Langel, E. Eriste, U. Langel, Cell-penetrating peptides: design, synthesis, and applications, ACS Nano 8 (2014) 1972–1994.
[9] J. Kreuter, Nanoparticles, in: J. Kreuter (Ed.), Colloidal drug delivery systems, Marcel Dekker, New York, 1994, pp. 219–342.
[10] C. Vauthier, K. Bouchemal, Methods for the preparation and manufacture of polymeric nanoparticles, Pharm. Res. 26 (2009) 1025–1058.
[11] B. Rihova, Biocompatibility of biomaterials: hemocompatibility, immunocompatibility and biocompatibility of solid polymeric materials and soluble targetable polymeric carriers, Adv. Drug Deliv. Rev. 21 (1996) 157–176.
[12] R. Duncan, The dawning era of polymer therapeutics, Nat. Rev. Drug Discov. 2 (2003) 347–360.
[13] R. Duncan, M.J. Vicent, Polymer therapeutics-prospects for 21st century: the end of the beginning, Adv. Drug Deliv. Rev. 65 (2013) 60–70.
[14] V.P. Torchilin, Micellar nanocarriers: pharmaceutical perspectives, Pharm. Res. 24 (2007) 1–16.
[15] R.R. Sawant, V.P. Torchilin, Liposomes as 'smart' pharmaceutical nanocarriers, Soft Matter 6 (2010) 4026–4044.
[16] H. Herd, N. Daum, A.T. Jones, H. Huwer, H. Ghandehari, C.M. Lehr, Nanoparticle geometry and surface orientation influence mode of cellular uptake, ACS Nano 7 (2013) 1961–1973.
[17] V.P. Torchilin, Fluorescence microscopy to follow the targeting of liposomes and micelles to cells and their intracellular fate, Adv. Drug Deliv. Rev. 57 (2005) 95–109.
[18] M. Diem, M. Romeo, S. Boydston-White, M. Miljković, C. Matthäus, A decade of vibrational micro-spectroscopy of human cells and tissue (1994–2004), Analyst 129 (2004) 880–885.
[19] C.V. Raman, K.S. Krishnan, A new type of secondary radiation, Nature 121 (1928) 501–502.
[20] G.J. Puppels, F.F.M. De Mul, C. Otto, J. Greve, M. Robert-Nicoud, D.J. Arndt-Jovin, T.M. Jovin, Studying single living cells and chromosomes by confocal Raman microspectroscopy, Nature 347 (1990) 301–303.
[21] K. Hamada, K. Fujita, N.I. Smith, M. Kobayashi, Y. Inouye, S. Kawata, Raman microscopy for dynamic molecular imaging of living cells, J. Biomed. Opt. 13 (2008) 044027.
[22] G.J. Puppels, J.H.F. Olminkhof, G.M.J. Segers-Nolten, C. Otto, F.F.M. De Mul, J. Greve, Laser irradiation and Raman spectroscopy of single living cells and chromosomes: sample degradation occurs with 514.5 nm but not with 660 nm laser light, Exp. Cell Res. 195 (1991) 361–367.
[23] I. Notingher, S. Verrier, H. Romanska, A.E. Bishop, J.M. Polak, L.L. Hench, In situ characterisation of living cells by Raman spectroscopy, Spectroscopy 16 (2002) 43–51.
[24] R. Wolthuis, T.C. Bakker Schut, P.J. Caspers, H.P.J. Bushman, T.J. Romer, H.A. Bruining, G.J. Puppels, Raman spectroscopic methods for in vitro and in vivo tissue characterization, in: W.T. Mason (Ed.), Fluorescent and Luminescent Probes for Biological Activity, Academic Press, London, 1999, pp. 433–455.
[25] A.F. Palonpon, J. Ando, H. Yamakoshi, K. Dodo, M. Sodeoka, S. Kawata, K. Fujita, Raman and SERS microscopy for molecular imaging of live cells, Nat. Protoc. 8 (2013) 677–692.
[26] C.B. Juang, L. Finzi, C.J. Bustamante, Design and application of a computer-controlled confocal scanning differential polarization microscope, Rev. Sci. Instrum. 59 (1988) 2399–2408.
[27] F. Draux, P. Jeannesson, A. Beljebbar, A. Tfayli, N. Fourre, M. Manfait, J. Sule-Suso, G.D. Sockalingum, Raman spectral imaging of single living cancer cells: a preliminary study, Analyst 134 (2009) 542–548.
[28] N. Uzunbajakava, A. Lenferink, Y. Kraan, B. Willekens, G. Vrensen, J. Greve, C. Otto, Nonresonant Raman imaging of protein distribution in single human cells, Biopolymers 72 (2003) 1–9.
[29] A. Ashkin, J.M. Dziedzic, T. Yamane, Optical trapping and manipulation of single cells using infrared laser beams, Nature 30 (1987) 769–771.
[30] D.G. Grier, A revolution in optical manipulation, Nature 424 (2003) 810–816.

[31] R. Liu, D.S. Taylor, D.L. Matthews, J.W. Chan, Parallel analysis of individual biological cells using multifocal laser tweezers Raman spectroscopy, Appl. Spectrosc. 64 (2010) 1308–1310.
[32] L. Kong, J. Chan, A rapidly modulated multifocal detection scheme for parallel acquisition of raman spectra from a 2-D focal array, Anal. Chem. 86 (2014) 6604–6609.
[33] C. Creely, G. Volpe, G. Singh, M. Soler, D. Petrov, Raman imaging of floating cells, Opt. Express 13 (2005) 6105–6110.
[34] M. Okuno, H.O. Hamaguchi, Multifocus confocal Raman microspectroscopy for fast multimode vibrational imaging of living cells, Opt. Lett. 35 (2010) 4096–4098.
[35] L. Kong, P. Zhang, J. Yu, P. Setlow, Y.Q. Li, Rapid confocal Raman imaging using a synchro multifoci-scan scheme for dynamic monitoring of single living cells, Appl. Phys. Lett. 98 (2011).
[36] F. Draux, C. Gobinet, J. Sule-Suso, A. Trussardi, M. Manfait, P. Jeannesson, G.D. Sockalingum, Raman spectral imaging of single cancer cells: probing the impact of sample fixation methods, Anal. Bioanal. Chem. 397 (2010) 2727–2737.
[37] J.W. Chan, D.S. Taylor, D.L. Thompson, The effect of cell fixation on the discrimination of normal and leukemia cells with laser tweezers Raman spectroscopy, Biopolymers 91 (2009) 132–139.
[38] S.O. Konorov, H.G. Schulze, N.J. Caron, J.M. Piret, M.W. Blades, R.F.B. Turner, Raman microspectroscopic evidence that dry-fixing preserves the temporal pattern of non-specific differentiation in live human embryonic stem cells, J. Raman Spectrosc. 42 (2011) 576–579.
[39] M.M. Mariani, P. Lampen, J. Popp, B.R. Wood, V. Deckert, Impact of fixation on in vitro cell culture lines monitored with Raman spectroscopy, Analyst 134 (2009) 1154–1161.
[40] V. Ranc, J. Srovnal, L. Kvitek, M. Hajduch, Discrimination of circulating tumor cells of breast cancer and colorectal cancer from normal human mononuclear cells using Raman spectroscopy, Analyst 138 (2013) 5983–5988.
[41] P. Lasch, Spectral pre-processing for biomedical vibrational spectroscopy and microspectroscopic imaging, Chemom. Intell. Lab. Syst. 117 (2012) 100–114.
[42] M. Hedegaard, C. Matthäus, S. Hassing, C. Krafft, M. Diem, J. Popp, Spectral unmixing and clustering algorithms for assessment of single cells by Raman microscopic imaging, Theor. Chem. Accounts 130 (2011) 1249–1260.
[43] M. Miljković, T. Chernenko, M.J. Romeo, B. Bird, C. Matthäus, M. Diem, Label-free imaging of human cells: algorithms for image reconstruction of Raman hyperspectral datasets, Analyst 135 (2010) 2002–2013.
[44] H.J. van Manen, Y.M. Kraan, D. Roos, C. Otto, Single-cell Raman and fluorescence microscopy reveal the association of lipid bodies with phagosomes in leukocytes, Proc. Natl. Acad. Sci. U. S. A. 102 (2005) 10159–10164.
[45] J.M. Benevides, M. Tsuboi, J.K.H. Bamford, G.J. Thomas, Polarized Raman spectroscopy of double-stranded RNA from bacteriophage phi 6: local Raman tensors of base and backbone vibrations, Biophys. J. 72 (1997) 2748–2762.
[46] D. Borchman, D.X. Tang, M.C. Yappert, Lipid composition, membrane structure relationships in lens and muscle sarcoplasmic reticulum membranes, Biospectroscopy 5 (1999) 151–167.
[47] K.R. Hightower, The role of the lens epithelium in development of Uv cataract, Curr. Eye Res. 14 (1995) 71–78.
[48] C. Krafft, W. Hinrichs, P. Orth, W. Saenger, H. Welfle, Interaction of Tet repressor with operator DNA and with tetracycline studied by infrared and Raman spectroscopy, Biophys. J. 74 (1998) 63–71.
[49] C. Matthäus, T. Chernenko, J.A. Newmark, C.M. Warner, M. Diem, Label-free detection of mitochondrial distribution in cells by nonresonant Raman microspectroscopy, Biophys. J. 93 (2007) 668–673.
[50] Z. Movasaghi, S. Rehman, I.U. Rehman, Raman spectroscopy of biological tissues, Appl. Spectrosc. Rev. 42 (2007) 493–541.
[51] I. Notingher, J. Selvakumaran, L.L. Hench, New detection system for toxic agents based on continuous spectroscopic monitoring of living cells, Biosens. Bioelectron. 20 (2004) 780–789.
[52] G.J. Thomas, J.M. Benevides, S.A. Overman, T. Ueda, K. Ushizawa, M. Saitoh, M. Tsuboi, Polarized Raman-spectra of oriented fibers of a-DNA and B-DNA — anisotropic and isotropic local Raman tensors of base and backbone vibrations, Biophys. J. 68 (1995) 1073–1088.
[53] R. Tuma, J.H.K. Bamford, D.H. Bamford, G.J. Thomas, Structure, interactions and dynamics of PRD1 virus.2. Organization of the viral membrane and DNA, J. Mol. Biol. 257 (1996) 102–115.
[54] I.W. Schie, L. Alber, A.L. Gryshuk, J.W. Chan, Investigating drug induced changes in single, living lymphocytes based on Raman micro-spectroscopy, Analyst 139 (2014) 2726–2733.
[55] I. Notingher, I. Bisson, A.E. Bishop, W.L. Randle, J.M.P. Polak, L.L. Hench, In situ spectral monitoring of mRNA translation in embryonic stem cells during differentiation in vitro, Anal. Chem. 76 (2004) 3185–3193.
[56] I. Notingher, I. Bisson, J.M. Polak, L.L. Hench, In situ spectroscopic study of nucleic acids in differentiating embryonic stem cells, Vib. Spectrosc. 35 (2004) 199–203.
[57] J.W. Chan, D.K. Lieu, T. Huser, R.A. Li, Label-free separation of human embryonic stem cells and their cardiac derivatives using Raman spectroscopy, Anal. Chem. 81 (2009) 1324–1331.
[58] E. Zuser, T. Chernenko, J. Newmark, M. Miljković, M. Diem, Confocal Raman microspectral imaging (CRMI) of murine stem cell colonies, Analyst 135 (2010) 3030–3033.
[59] S.O. Konorov, H.G. Schulze, J.M. Piret, M.W. Blades, R.F. Turner, Label-free determination of the cell cycle phase in human embryonic stem cells by Raman microspectroscopy, Anal. Chem. 85 (2013) 8996–9002.
[60] S.O. Konorov, H.G. Schulze, J.M. Piret, R.F.B. Turner, M.W. Blades, Evidence of marked glycogen variations in the characteristic Raman signatures of human embryonic stem cells, J. Raman Spectrosc. 42 (2011) 1135–1141.
[61] S.O. Konorov, H.G. Schulze, C.G. Atkins, J.M. Piret, S.A. Aparicio, R.F.B. Turner, M.W. Blades, Absolute quantification of intracellular glycogen content in human embryonic stem cells with Raman microspectroscopy, Anal. Chem. 83 (2011) 6254–6258.
[62] Y. Tan, S.O. Konorov, H.G. Schulze, J.M. Piret, M.W. Blades, R.F.B. Turner, Comparative study using Raman microspectroscopy reveals spectral signatures of human induced pluripotent cells more closely resemble those from human embryonic stem cells than those from differentiated cells, Analyst 137 (2012) 4509–4515.
[63] S. Caponi, L. Liguori, A. Giugliarelli, M. Mattarelli, A. Morresi, P. Sassi, L. Urbanelli, C. Musio, Raman micro-spectroscopy: a powerful tool for the monitoring of dynamic supramolecular changes in living cells, Biophys. Chem. 182 (2013) 58–63.
[64] C. Krafft, T. Knetschke, A. Siegner, R.H.W. Funk, R. Salzer, Mapping of single cells by near infrared Raman microspectroscopy, Vib. Spectrosc. 32 (2003) 75–83.
[65] K.W. Short, S. Carpenter, J.P. Freyer, J.R. Mourant, Raman spectroscopy detects biochemical changes due to proliferation in mammalian cell cultures, Biophys. J. 88 (2005) 4274–4288.
[66] E.O. Potma, W.P. De Boeij, P.J.M. Van Haastert, D.A. Wiersma, Real-time visualization of intracellular hydrodynamics in single living cells, Proc. Natl. Acad. Sci. U. S. A. 98 (2001) 1577–1582.
[67] H. Fukunaga, H. Yoshimura, Y. Nishina, Y. Nagashima, M. Tachibana, Label-free biomedical imaging of hydrodynamics in single human cells, Biomed. Res. 31 (2010) 177–181.
[68] T.J. Moritz, D.S. Taylor, D.M. Krol, J. Fritch, J.W. Chan, Detection of doxorubicin-induced apoptosis of leukemic T-lymphocytes by laser tweezers Raman spectroscopy, Biomed. Opt. Express 1 (2010) 1138–1147.
[69] N. Uzunbajakava, A. Lenferink, Y. Kraan, E. Volokhina, G. Vrensen, J. Greve, C. Otto, Nonresonant confocal Raman imaging of DNA and protein distribution in apoptotic cells, Biophys. J. 84 (2003) 3968–3981.
[70] C. Krafft, T. Knetschke, R.H.W. Funk, R. Salzer, Identification of organelles and vesicles in single cells by Raman microspectroscopic mapping, Vib. Spectrosc. 38 (2005) 85–93.
[71] C. Krafft, T. Knetschke, R.H.W. Funk, R. Salzer, Studies on stress-induced changes at the subcellular level by Raman microspectroscopic mapping, Anal. Chem. 78 (2006) 4424–4429.
[72] K. Majzner, K. Kochan, N. Kachamakova-Trojanowska, E. Maslak, S. Chlopicki, M. Baranska, Raman imaging providing insights into chemical composition of lipid droplets of different size and origin: in hepatocytes and endothelium, Anal. Chem. 86 (2014) 6666–6674.
[73] C. Stiebing, C. Matthäus, C. Krafft, A.A. Keller, K. Weber, S. Lorkowski, J. Popp, Complexity of fatty acid distribution inside human macrophages on single cell level using Raman micro-spectroscopy, Anal. Bioanal. Chem. 406 (2014) 7037–7046.
[74] L. Tirinato, C. Liberale, S. Di Franco, P. Candeloro, A. Benfante, R. La Rocca, L. Potze, R. Marotta, R. Ruffilli, V.P. Rajamanickam, M. Malerba, F. De Angelis, A. Falqui, E. Carbone, M. Todaro, J.P. Medema, G. Stassi, E. Di Fabrizio, Lipid droplets: a new player in colorectal cancer stem cells unveiled by spectroscopic imaging, Stem Cells 33 (2015) 35–44.
[75] S. Yue, J. Li, S.-Y. Lee, Hyeon J. Lee, T. Shao, B. Song, L. Cheng, Timothy A. Masterson, X. Liu, Timothy L. Ratliff, J.-X. Cheng, Cholesteryl ester accumulation induced by PTEN loss and PI3K/AKT activation underlies human prostate cancer aggressiveness, Cell Metab. 19 (2014) 393–406.
[76] H.G. Schulze, S.O. Konorov, J.M. Piret, M.W. Blades, R.F. Turner, Label-free imaging of mammalian cell nucleoli by Raman microspectroscopy, Analyst 138 (2013) 3416–3423.
[77] M. Derenzini, L. Montanaro, D. Treré, What the nucleolus says to a tumour pathologist, Histopathology 54 (2009) 753–762.
[78] V.V. Pully, A.T.M. Lenferink, C. Otto, Time-lapse Raman imaging of single live lymphocytes, J. Raman Spectrosc. 42 (2011) 167–173.
[79] K. Meister, D.A. Schmidt, E. Brundermann, M. Havenith, Confocal Raman microspectroscopy as an analytical tool to assess the mitochondrial status in human spermatozoa, Analyst 135 (2010) 1370–1374.
[80] Z. Huang, G. Chen, X. Chen, J. Wang, J. Chen, P. Lu, R. Chen, Rapid and label-free identification of normal spermatozoa based on image analysis and micro-Raman spectroscopy, J. Biophotonics 7 (2014) 671–675.
[81] T. Huser, C.A. Orme, C.W. Hollars, M.H. Corzett, R. Balhorn, Raman spectroscopy of DNA packaging in individual human sperm cells distinguishes normal from abnormal cells, J. Biophotonics 2 (2009) 322–332.
[82] H. Wang, T.H. Tsai, J. Zhao, A.M. Lee, B.K. Lo, M. Yu, H. Lui, D.I. McLean, H. Zeng, Differentiation of HaCaT cell and melanocyte from their malignant counterparts using micro-Raman spectroscopy guided by confocal imaging, Photodermatol. Photoimmunol. Photomed. 28 (2012) 147–152.
[83] M.M. Mariani, L.J. Maccoux, C. Matthäus, M. Diem, J.G. Hengstler, V. Deckert, Micro-Raman detection of nuclear membrane lipid fluctuations in senescent epithelial breast cancer cells, Anal. Chem. 82 (2010) 4259–4263.
[84] L. Wei, F. Hu, Y. Shen, Z. Chen, Y. Yu, C.C. Lin, M.C. Wang, W. Min, Live-cell imaging of alkyne-tagged small biomolecules by stimulated Raman scattering, Nat. Methods 11 (2014) 410–412.
[85] H. Yamakoshi, K. Dodo, A. Palonpon, J. Ando, K. Fujita, S. Kawata, M. Sodeoka, Alkyne-tag Raman imaging for visualization of mobile small molecules in live cells, J. Am. Chem. Soc. 134 (2012) 20681–20689.
[86] H. Yamakoshi, K. Dodo, M. Okada, J. Ando, A. Palonpon, K. Fujita, S. Kawata, M. Sodeoka, Imaging of EdU, an alkyne-tagged cell proliferation probe, by Raman microscopy, J. Am. Chem. Soc. 133 (2011) 6102–6105.
[87] A. Salic, T.J. Mitchison, A chemical method for fast and sensitive detection of DNA synthesis in vivo, Proc. Natl. Acad. Sci. U. S. A. 105 (2008) 2415–2420.
[88] Y. Enomoto, K. Enomoto, T. Kitamura, T. Kanda, Keratinocyte-specific POU transcription factor hSkn-1a represses the growth of cervical cancer cell lines, Oncogene 23 (2004) 5014–5022.

[89] Z.M. Mu, X.F. Le, S. Vallian, A.B. Glassman, K.S. Chang, Stable overexpression of PML alters regulation of cell cycle progression in HeLa cells, Carcinogenesis 18 (1997) 2063–2069.
[90] H. Yamakoshi, A. Palonpon, K. Dodo, J. Ando, S. Kawata, K. Fujita, M. Sodeoka, A sensitive and specific Raman probe based on bisarylbutadiyne for live cell imaging of mitochondria, Bioorg. Med. Chem. Lett. 25 (2015) 664–667.
[91] S.F. El-Mashtoly, D. Petersen, H.K. Yosef, A. Mosig, A. Reinacher-Schick, C. Kotting, K. Gerwert, Label-free imaging of drug distribution and metabolism in colon cancer cells by Raman microscopy, Analyst 139 (2014) 1155–1161.
[92] H.J. van Manen, A. Lenferink, C. Otto, Noninvasive imaging of protein metabolic labeling in single human cells using stable isotopes and Raman microscopy, Anal. Chem. 80 (2008) 9576–9582.
[93] C. Matthäus, C. Krafft, B. Dietzek, B.R. Brehm, S. Lorkowski, J. Popp, Noninvasive imaging of intracellular lipid metabolism in macrophages by Raman microscopy in combination with stable isotopic labeling, Anal. Chem. 84 (2012) 8549–8556.
[94] C. Matthäus, A. Kale, T. Chernenko, V. Torchilin, M. Diem, New ways of imaging uptake and intracellular fate of liposomal drug carrier systems inside individual cells, based on raman microscopy, Mol. Pharm. 5 (2008) 287–293.
[95] T. Chernenko, R.R. Sawant, M. Miljkovic, L. Quintero, M. Diem, V. Torchilin, Raman microscopy for noninvasive imaging of pharmaceutical nanocarriers: intracellular distribution of cationic liposomes of different composition, Mol. Pharm. 9 (2012) 930–936.
[96] U. Edlund, A.C. Albertsson, Degradable polymer microspheres for controlled drug delivery, in: A.C. Albertsson (Ed.), Degradable Aliphatic Polyesters, Springer, Berlin Heidelberg, 2002, pp. 67–112.
[97] G. Schliecker, C. Schmidt, S. Fuchs, R. Wombacher, T. Kissel, Hydrolytic degradation of poly(lactide-co-glycolide) films: effect of oligomers on degradation rate and crystallinity, Int. J. Pharm. 266 (2003) 39–49.
[98] A.A. van Apeldoorn, H.J. van Manen, J.M. Bezemer, J.D. de Bruijn, C.A. van Blitterswijk, C. Otto, Raman imaging of PLGA microsphere degradation inside macrophages, J. Am. Chem. Soc. 126 (2004) 13226–13227.
[99] T. Chernenko, C. Matthäus, L. Milane, L. Quintero, M. Amiji, M. Diem, Label-free raman spectral imaging of intracellular delivery and degradation of polymeric nanoparticle systems, ACS Nano 3 (2009) 3552–3559.
[100] K.E. Uhrich, S.M. Cannizzaro, R.S. Langer, K.M. Shakesheff, Polymeric systems for controlled drug release, Chem. Rev. 99 (1999) 3181–3198.
[101] C.G. Pitt, Poly-ε-caprolactone and Its copolymers, in: R. Langer, C.M. (Eds.), Biodegradable Polymers as Drug Delivery Systems, Marcel Dekker Inc., New York, 1990, pp. 71–120.
[102] G. Romero, I. Estrela-Lopis, J. Zhou, E. Rojas, A. Franco, C.S. Espinel, A.G. Fernández, C. Gao, E. Donath, S.E. Moya, Surface engineered poly(lactide-co-glycolide) nanoparticles for intracellular delivery: uptake and cytotoxicity — a confocal Raman microscopic study, Biomacromolecules 11 (2010) 2993–2999.
[103] G. Romero, Y. Qiu, R.A. Murray, S.E. Moya, Study of intracellular delivery of doxorubicin from poly(lactide-co-glycolide) nanoparticles by means of fluorescence lifetime imaging and confocal raman microscopy, Macromol. Biosci. 13 (2013) 234–241.
[104] G. Romero, O. Ochoteco, D.J. Sanz, I. Estrela-Lopis, E. Donath, S.E. Moya, Poly(lactide-co-glycolide) nanoparticles, layer by layer engineered for the sustainable delivery of AntiTNF-α, Macromol. Biosci. 13 (2013) 903–912.
[105] C. Matthäus, S. Schubert, M. Schmitt, C. Krafft, B. Dietzek, U.S. Schubert, J. Popp, Resonance Raman spectral imaging of intracellular uptake of β-carotene loaded poly(D, L-lactide-co-glycolide) nanoparticles, ChemPhysChem 14 (2013) 155–161.
[106] P. Verderio, L. Pandolfi, S. Mazzucchelli, M.R. Marinozzi, R. Vanna, F. Gramatica, F. Corsi, M. Colombo, C. Morasso, D. Prosperi, Antiproliferative effect of ASC-J9 delivered by PLGA nanoparticles against estrogen-dependent breast cancer cells, Mol. Pharm. 11 (2014) 2864–2875.
[107] J. Ye, S.A. Fox, M. Cudic, E.M. Rezler, J.L. Lauer, G.B. Fields, A.C. Terentis, Determination of penetratin secondary structure in live cells with Raman microscopy, J. Am. Chem. Soc. 132 (2010) 980–988.
[108] S. Krimm, J. Bandekar, Vibrational spectroscopy and conformation of peptides, polypeptides, and proteins, Adv. Protein Chem. 38 (1986) 181–364.
[109] W.E. Huang, K. Stoecker, R. Griffiths, L. Newbold, H. Daims, A.S. Whiteley, M. Wagner, Raman-FISH: Combining stable-isotope Raman spectroscopy and fluorescence in situ hybridization for the single cell analysis of identity and function, Environ. Microbiol. 9 (2007) 1878–1889.
[110] T.E. Meyerrose, D.A. De Ugarte, A.A. Hofling, P.E. Herrbrich, T.D. Cordonnier, L.D. Shultz, J.C. Eagon, L. Wirthlin, M.S. Sands, M.A. Hedrick, J.A. Nolta, In vivo distribution of human adipose-derived mesenchymal stem cells in novel xenotransplantation models, Stem Cells 25 (2007) 220–227.
[111] J. Tolar, A.J. Nauta, M.J. Osborn, A.P. Mortari, R.T. McElmurry, S. Bell, L. Xia, N. Zhou, M. Riddle, T.M. Schroeder, J.J. Westendorf, R.S. McIvor, P.C.W. Hogendoorn, K. Szuhai, L. Oseth, B. Hirsch, S.R. Yant, M.A. Kay, A. Peister, D.J. Prockop, W.E. Fibbe, B.R. Blazar, Sarcoma derived from cultured mesenchymal stem cells, Stem Cells 25 (2007) 371–379.
[112] R. Yuste, Fluorescence microscopy today, Nat. Methods 2 (2005) 902–904.
[113] H. Mao, R. Cai, N. Kawazoe, G. Chen, Long-term stem cell labeling by collagen-functionalized single-walled carbon nanotubes, Nanoscale 6 (2014) 1552–1559.
[114] B.D. Holt, K.N. Dahl, M.F. Islam, Quantification of uptake and localization of bovine serum albumin-stabilized single-wall carbon nanotubes in different human cell types, Small 7 (2011) 2348–2355.
[115] M.J. O'Connell, S.H. Bachilo, C.B. Huffman, V.C. Moore, M.S. Strano, E.H. Haroz, K.L. Rialon, P.J. Boul, W.H. Noon, C. Kittrell, J. Ma, R.H. Hauge, R.B. Weisman, R.E. Smalley, Band gap fluorescence from individual single-walled carbon nanotubes, Science 297 (2002) 593–596.
[116] B.D. Holt, P.A. Short, A.D. Rape, Y.L. Wang, M.F. Islam, K.N. Dahl, Carbon nanotubes reorganize actin structures in cells and ex vivo, ACS Nano 4 (2010) 4872–4878.
[117] G. Romero, E. Rojas, I. Estrela-Lopis, E. Donath, S.E. Moya, Spontaneous confocal Raman microscopy—a tool to study the uptake of nanoparticles and carbon nanotubes into cells, Nanoscale Res. Lett. 6 (2011) 1–4.
[118] C.A. Puckett, J.K. Barton, Fluorescein redirects a ruthenium–octaarginine conjugate to the nucleus, J. Am. Chem. Soc. 131 (2009) 8738–8739.
[119] K. Meister, J. Niesel, U. Schatzschneider, N. Metzler-Nolte, D.A. Schmidt, M. Havenith, Label-free imaging of metal–carbonyl complexes in live cells by Raman microspectroscopy, Angew. Chem. Int. Ed. 49 (2010) 3310–3312.
[120] J. Niesel, A. Pinto, H.W. Peindy N'Dongo, K. Merz, I. Ott, R. Gust, U. Schatzschneider, Photoinduced CO release, cellular uptake and cytotoxicity of a tris(pyrazolyl)methane (tpm) manganese tricarbonyl complex, Chem. Commun. (2008) 1798–1800.
[121] L. Hartsuiker, W. Petersen, R.G. Rayavarapu, A. Lenferink, A.A. Poot, L.W.M.M. Terstappen, T.G. Van Leeuwen, S. Manohar, C. Otto, Raman and fluorescence spectral imaging of live breast cancer cells incubated with PEGylated gold nanorods, Appl. Spectrosc. 66 (2012) 66–74.
[122] B. Kann, B.J. Teubl, E. Roblegg, M. Windbergs, Label-free in vitro visualization of particle uptake into human oral buccal epithelial cells by confocal Raman microscopy, Analyst 139 (2014) 5069–5074.
[123] L. Ahlinder, B. Ekstrand-Hammarstrom, P. Geladi, L. Osterlund, Large uptake of titania and iron oxide nanoparticles in the nucleus of lung epithelial cells as measured by Raman imaging and multivariate classification, Biophys. J. 105 (2013) 310–319.
[124] D.L. Jeanmaire, R.P. Van Duyne, Surface Raman spectroelectrochemistry Part I. Heterocyclic, aromatic, and aliphatic amines adsorbed on the anodized silver electrode, J. Electroanal. Chem. 84 (1977) 1–20.
[125] M. Kerker, Electromagnetic model for surface-enhanced Raman scattering (SERS) on metal colloids, Acc. Chem. Res. 17 (1984) 271–277.
[126] M.K. Gregas, F. Yan, J. Scaffidi, H.N. Wang, T. Vo-Dinh, Characterization of nanoprobe uptake in single cells: spatial and temporal tracking via SERS labeling and modulation of surface charge, Nanomedicine 7 (2011) 115–122.
[127] J. Kneipp, H. Kneipp, M. McLaughlin, D. Brown, K. Kneipp, In vivo molecular probing of cellular compartments with gold nanoparticles and nanoaggregates, Nano Lett. 6 (2006) 2225–2231.
[128] K. Kneipp, A.S. Haka, H. Kneipp, K. Badizadegan, N. Yoshizawa, C. Boone, K.E. Shafer-Peltier, J.T. Motz, R.R. Dasari, M.S. Feld, Surface-enhanced raman spectroscopy in single living cells using gold nanoparticles, Appl. Spectrosc. 56 (2002) 150–154.
[129] A. Sujith, T. Itoh, H. Abe, A.A. Anas, K. Yoshida, V. Biju, M. Ishikawa, Surface enhanced Raman scattering analyses of individual silver nanoaggregates on living single yeast cell wall, Appl. Phys. Lett. 92 (2008).
[130] L. Xiao, S. Harihar, D.R. Welch, A. Zhou, Imaging of epidermal growth factor receptor on single breast cancer cells using surface-enhanced Raman spectroscopy, Anal. Chim. Acta 843 (2014) 73–82.
[131] J. Fang, S. Du, S. Lebedkin, Z. Li, R. Kruk, M. Kappes, H. Hahn, Gold mesostructures with tailored surface topography and their self-assembly arrays for surface-enhanced Raman spectroscopy, Nano Lett. 10 (2010) 5006–5013.
[132] Z. Wang, J. Zhang, J.M. Ekman, P.J.A. Kenis, Y. Lu, DNA-mediated control of metal nanoparticle shape: one-pot synthesis and cellular uptake of highly stable and functional gold nanoflowers, Nano Lett. 10 (2010) 1886–1891.
[133] J. Xie, Q. Zhang, J.Y. Lee, D.I.C. Wang, The synthesis of SERS-active gold nanoflower tags for in vivo applications, ACS Nano 2 (2008) 2473–2480.
[134] Q. Li, Y. Jiang, R. Han, X. Zhong, S. Liu, Z.Y. Li, Y. Sha, D. Xu, High surface-enhanced Raman scattering performance of individual gold nanoflowers and their application in live cell imaging, Small 9 (2013) 927–932.
[135] A.M. Fales, H. Yuan, T. Vo-Dinh, Silica-coated gold nanostars for combined surface-enhanced Raman scattering (SERS) detection and singlet-oxygen generation: a potential nanoplatform for theranostics, Langmuir 27 (2011) 12186–12190.
[136] H. Yuan, A.M. Fales, C.G. Khoury, J. Liu, T. Vo-Dinh, Spectral characterization and intracellular detection of surface-enhanced Raman scattering (SERS)-encoded plasmonic gold nanostars, J. Raman Spectrosc. 44 (2013) 234–239.
[137] A.M. Fales, H. Yuan, T. Vo-Dinh, Cell-penetrating peptide enhanced intracellular Raman imaging and photodynamic therapy, Mol. Pharm. 10 (2013) 2291–2298.
[138] Z. Wang, S. Pan, T.D. Krauss, H. Du, L.J. Rothberg, The structural basis for giant enhancement enabling single-molecule Raman scattering, Proc. Natl. Acad. Sci. U. S. A. 100 (2003) 8638–8643.
[139] N.A. Brazhe, E.Y. Parshina, V.V. Khabatova, A.A. Semenova, A.R. Brazhe, A.I. Yusipovich, A.S. Sarycheva, A.A. Churin, E.A. Goodilin, G.V. Maksimov, O.V. Sosnovtseva, Tuning SERS for living erythrocytes: focus on nanoparticle size and plasmon resonance position, J. Raman Spectrosc. 44 (2013) 686–694.
[140] Z. Liu, Z. Guo, H. Zhong, X. Qin, M. Wan, B. Yang, Graphene oxide based surface-enhanced Raman scattering probes for cancer cell imaging, Phys. Chem. Chem. Phys. 15 (2013) 2961–2966.
[141] L. Jiang, J. Qian, F. Cai, S. He, Raman reporter-coated gold nanorods and their applications in multimodal optical imaging of cancer cells, Anal. Bioanal. Chem. 400 (2011) 2793–2800.
[142] G. Von Maltzahn, A. Centrone, J.H. Park, R. Ramanathan, M.J. Sailor, T. Alan Hatton, S.N. Bhatia, SERS-coded cold nanorods as a multifunctional platform for densely multiplexed near-infrared imaging and photothermal heating, Adv. Mater. 21 (2009) 3175–3180.
[143] D. Pan, J. Zhang, Z. Li, M. Wu, Hydrothermal route for cutting graphene sheets into blue-luminescent graphene quantum dots, Adv. Mater. 22 (2010) 734–738.
[144] J. Shen, Y. Zhu, C. Chen, X. Yang, C. Li, Facile preparation and upconversion luminescence of graphene quantum dots, Chem. Commun. 47 (2011) 2580–2582.
[145] M. Zhang, L. Bai, W. Shang, W. Xie, H. Ma, Y. Fu, D. Fang, H. Sun, L. Fan, M. Han, C. Liu, S. Yang, Facile synthesis of water-soluble, highly fluorescent graphene

quantum dots as a robust biological label for stem cells, J. Mater. Chem. 22 (2012) 7461–7467.
[146] Q. Liu, L. Wei, J. Wang, F. Peng, D. Luo, R. Cui, Y. Niu, X. Qin, Y. Liu, H. Sun, J. Yang, Y. Li, Cell imaging by graphene oxide based on surface enhanced Raman scattering, Nanoscale 4 (2012) 7084–7089.
[147] X. Ma, Q. Qu, Y. Zhao, Z. Luo, Y. Zhao, K.W. Ng, Y. Zhao, Graphene oxide wrapped gold nanoparticles for intracellular Raman imaging and drug delivery, J. Mater. Chem. B 1 (2013) 6495–6500.
[148] K.V. Kong, Z. Lam, W.D. Goh, W.K. Leong, M. Olivo, Metal carbonyl–gold nanoparticle conjugates for live-cell SERS imaging, Angew. Chem. Int. Ed. 51 (2012) 9796–9799.
[149] S. Lee, H. Chon, J. Lee, J. Ko, B.H. Chung, D.W. Lim, J. Choo, Rapid and sensitive phenotypic marker detection on breast cancer cells using surface-enhanced Raman scattering (SERS) imaging, Biosens. Bioelectron. 51 (2014) 238–243.
[150] Y. Li, X. Qi, C. Lei, Q. Yue, S. Zhang, Simultaneous SERS detection and imaging of two biomarkers on the cancer cell surface by self-assembly of branched DNA–gold nanoaggregates, Chem. Commun. 50 (2014) 9907–9909.
[151] V.P. Torchilin, Tat peptide-mediated intracellular delivery of pharmaceutical nanocarriers, Adv. Drug Deliv. Rev. 60 (2008) 548–558.
[152] N. Shaklai, J. Yguerabide, H.M. Ranney, Classification and localization of hemoglobin binding sites on the red blood cell membrane, Biochemistry 16 (1977) 5593–5597.
[153] N. Shaklai, J. Yguerabide, H.M. Ranney, Interaction of hemoglobin with red blood cell membranes as shown by a fluorescent chromophore, Biochemistry 16 (1977) 5585–5592.
[154] W. Xie, L. Wang, Y. Zhang, L. Su, A. Shen, J. Tan, J. Hu, Nuclear targeted nanoprobe for single living cell detection by surface-enhanced Raman scattering, Bioconjug. Chem. 20 (2009) 768–773.
[155] Š. Bálint, S. Rao, M.M. Sánchez, V. Huntošová, P. Miškovský, D. Petrov, Diffusion and cellular uptake of drugs in live cells studied with surface-enhanced Raman scattering probes, J. Biomed. Opt. 15 (2010) 027005.
[156] K. Fujita, S. Ishitobi, K. Hamada, N.I. Smith, A. Taguchi, Y. Inouye, S. Kawata, Time-resolved observation of surface-enhanced Raman scattering from gold nanoparticles during transport through a living cell, J. Biomed. Opt. 14 (2009) 024038.